Feel free to get in contact: geo.david.fernandez@gmail.com

Models show a mechanism where forearc sediments thermally activate deep crustal flow

Viscous flow changes regional subsidence into short-wavelength uplift/subsidence

Forearc high uplift is controlled by sediment accretion, sedimentation and temperature

Mechanism explains S Anatolia upper-plate strain and vertical motions in Neogene

Mechanism explains S Turkey uplift by accretion and viscous flow, not slab break-off

Forearc high uplift by lower crustal flow during growth of the Cyprus-Anatolian margin

***David Fernández-Blanco*[1]*, Utsav Mannu*[2,3]*, Giovanni Bertotti*[1]*, and Sean D. Willett*[4]**

[1] *Department of Geoscience and Engineering, Faculty of Civil Engineering and Geosciences, Delft, University of Technology, Stevinweg 1, 2628CN, Delft, the Netherlands*
geo.david.fernandez@gmail.com
[2] *Earthquake and Volcano Information, Earthquake Research Institute, Tokyo University.*
[3] *Department of Earth & Climate, Indian Institute of Science Education and Research, Pune.*
[4] *Geological Institute, Swiss Federal Institute of Technology, 8092 Zurich, Switzerland.*

Abstract

We present a model for the dynamic formation of the forearc high of southern Anatolia where sedimentation in the forearc basin leads to thermally-activated deformation in the lower crust. Our thermo-mechanical models demonstrate that forearc sedimentation increases the temperature of the underlying crust by “blanketing” the heat flux and increasing Moho depth. Deformation switches from frictional to viscous with a higher strain rate led by increased temperature. Viscous deformation changes large-wavelength subsidence into coeval, short-wavelength uplift and subsidence. Models show that forearc highs are intrinsic to accretionary wedges and can grow dynamically and non-linearly at rates dependent on sediment accretion, sedimentation and temperature. The mechanism explains the uplift of the Central Anatolian Plateau southern margin and the Neogene vertical motions and upper-plate strain in the Anatolian margin along Central Cyprus. This system is analogous to forearc highs in other mature accretionary margins, like Cascadia, Lesser Antilles or Makran.

keywords: outer-arc high; accretionary wedge; orogenic plateau; plateau margin; Central Anatolian Plateau

1 Introduction

Geodynamic processes are the first-order drivers of topography in orogenic plateaus and plateau margins. However, mechanisms for detailed patterns of uplift in orogenic plateau systems, such as Himalaya-Tibet and Puna-Altiplano (e.g., Allmendinger et al., 1997; Molnar, 1984) remain diverse and difficult to generalize. This is also true for the history of topography growth of the orogenic plateau of Central Anatolia and its margins. Whereas continental delamination (Bartol and Govers, 2014) or lithospheric drip (Göğüş et al., 2017) have been suggested to sustain Central Anatolia low relief at ~1 km, its plateau margins are geodynamically different; transpressional orogenic uplift may have formed the northern margin (Yildirim et al., 2011), and the southern margin is strongly influenced by the Cyprus subduction zone to the south. The formation mechanism of the latter is of particular interest, for the uplift in the southern margin has a limited N-S extent and occurred in the absence of regional accommodating faults (Fernández-Blanco et al., 2019) (Fig. 1).

Contrasting models are proposed to explain the uplift of the southern margin of the Central Anatolian Plateau (SCAP) (Fig. 1). A set of studies have proposed various multi-phase uplift scenarios with increased uplift rates in time led by a succession of events including, or linked with, slab break-off events that vary in time and/or depth (e.g., Cosentino et al., 2012; Öğretmen et al., 2018; Schildgen et al., 2014, 2012). These studies constrain depositional age or subaerial exposure of rocks at specific sites (Fig. 1C), and are compatible with the thinned Central Anatolian lithosphere inferred from seismic tomography (Mutlu and Karabulut, 2011). However, proposed geodynamic scenarios overlook evidence that suggests the mechanism is not likely to be active over the entire E-W extent of the Taurides, i.e. the presence of the African slab below the modern Central Taurides and the substantial thickness of the Anatolian crust and lithosphere there (e.g., Abgarmi et al., 2017; Bakırcı et al., 2012; Biryol et al., 2011; Delph et al., 2017). A different set of studies accounting for geological constraints and geophysical observables propose crustal thickening as an alternative mechanism to explain the uplift and elevation of the plateau margin (Fernández-Blanco 2014; Fernández-Blanco et al., 2019; Meijers et al., 2018; Walsh-Kennedy et al., 2014). The latter studies are based on reflection seismic data, field evidence and stable isotope paleoaltimetry estimates (Fig. 1C), and are compatible with the boundaries and short wavelength of margin uplift and seaward subsidence in South Turkey (~100 km from the deepest bathymetry to the highest topography). Yet, these studies have not provided a detailed explanation of the crustal thickening mechanism nor the timing and position of uplift implied by the occurrence of raised marine sediments.

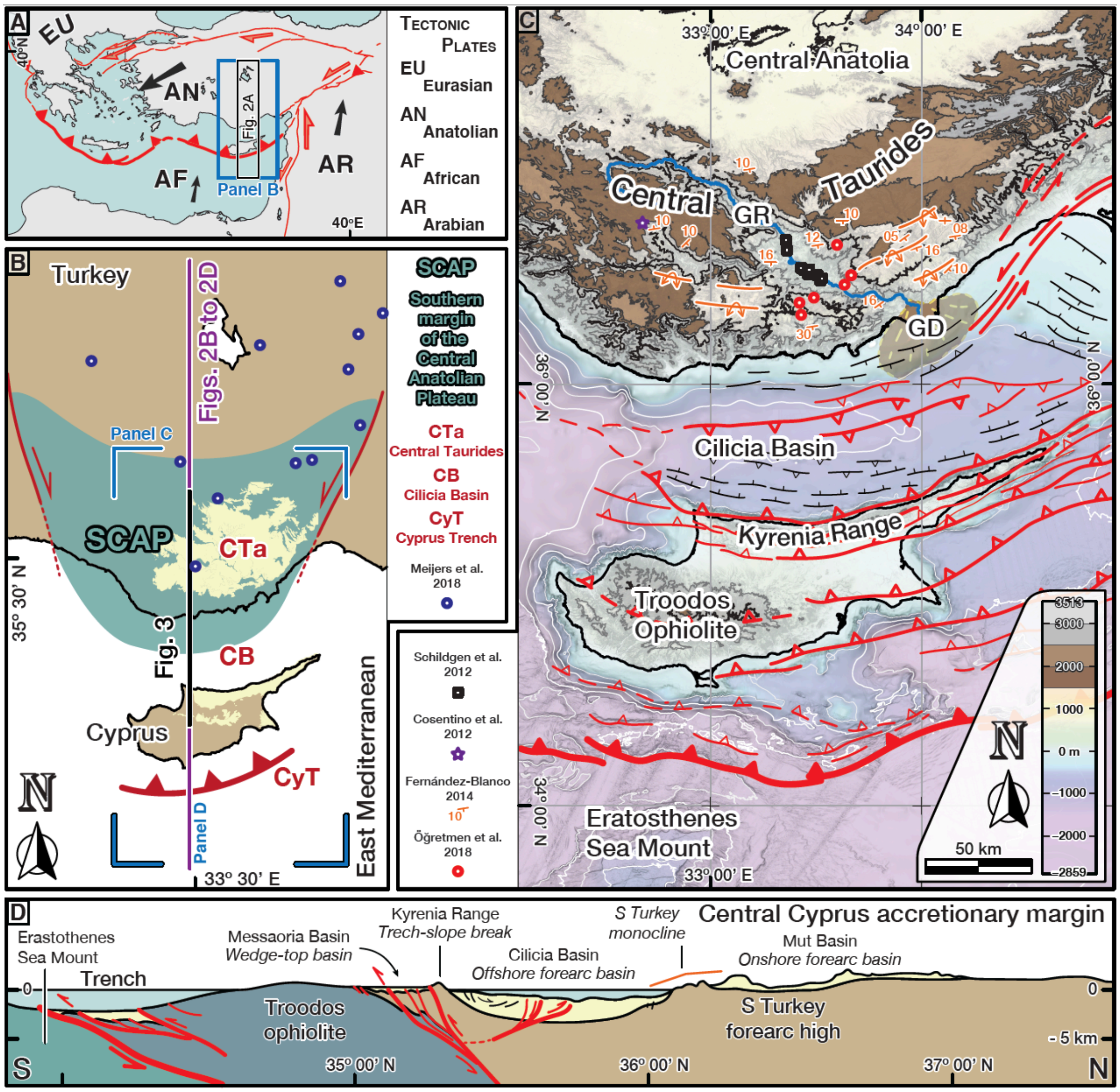

Figure 1. *Central Cyprus subduction zone and its surrounding tectonic frame.* ***(A)*** *Regional map showing the motion of the African (AF), Arabian (AR) and Anatolian (AN) tectonic plates with respect to Eurasia (EU), and the location of panel B below and Fig. 2A.* ***(B)*** *Map of the northeast Mediterranean, showing the extent of the southern margin of the Central Anatolian Plateau (SCAP) and other key elements in the area. CTa = Central Taurides; CB = Cilicia Basin; CyT = Cyprus trench. Neogene rocks on Central Taurides and Cyprus are in yellow. The location of the part of the data set of Meijers et al. (2018) that falls within the map area is shown as blue circles. The location of panel C to the right and panel D below*

are also shown, as well as that of transects in Fig. 2B to 2D and Fig. 3. ***(C)*** *Map of the Central Cyprus accretionary margin and surrounding regions. The offshore bathymetry in a graded color hillshade shows shallowing from purple to blue. Offshore structures come from Aksu et al. (2005) and Calon et al. (2005) and are classified into 4 hierarchical levels; the subduction megathrust in the south, regional structures in thick red, secondary structures in thin red and minor structures in black. The topography in the onshore, including the Central Taurides, is shown as a colored graded hillshade until 1.5 km with the 1 km equal-height contour highlighted in black, in brown from 1.5 km to 2.5 km, and in grey for heights >2.5 km. Structural data from Fernández-Blanco (2014) in orange shows bedding dips in Late Miocene marine rocks and the S Turkey monocline delineated by them. The location of data sets of Cosentino et al. (2012), Schildgen et al. (2012) and Öğretmen et al. (2018) are shown as a purple star, black squares, and red circles, respectively. GR and GD stand for Göksu River and Göksu Delta.* ***(D)*** *Cross-section across the Central Cyprus accretionary margin showing the main elements along the margin and their correlation with elements of accretionary wedges. Modified from Fernández-Blanco et al.* (2019)*.*

An uplift mechanism occurs during forearc deformation of an orogenic wedge (Platt, 1986; Willett et al. 1993) when lower crustal flow leads to uplift of an outer-arc or forearc high in the forearc region. Forearc high uplift by deep-seated flow is proposed for the accretionary margins of the Lesser Antilles, Cascadia and others (e.g., Pavlis and Bruhn, 1983; Williams et al., 1994). The development of a preceding forearc basin that is later fragmented by the uplift of the forearc high has been suggested for Cascadia (McNeill et al., 2000), and has been predicted by mechanistic critical wedge models with plastic-viscous rheology (Fuller et al., 2006). In these models, the forearc basin grows through stabilization of the wedge by sediment loading on wedge-segments with a landward critical surface slope, forming a so-called negative-alpha basin (Willett and Schlunegger, 2010) that has no internal deformation and is restricted by its bounding highs. Protracted growth of a negative-alpha basin in the forearc leads to crustal thickening, which may promote thermal activation of viscous flow at the base of the crust and a later stage uplift of the forearc high (Fuller et al., 2006).

Here, we explore the role of wedge-top sedimentation on forearc dynamics for conditions applicable to the Cyprus-Anatolia margin. We use transects of the Central Cyprus subduction margin and its forearc, derived by integration of geophysical and geological data, to constraint coupled thermo-mechanical, visco-plastic numerical models. A notable transition emerges in these models as accretionary growth and sediment deposition produce a "thermal blanketing" effect increasing the thermal resistance of the crust, leading to higher temperatures and thermally weakening the upper plate. In this context, a forearc high grows dynamically and non-linearly as an integral part of the accreting wedge and upper plate crust, seaward of any continental backstop. This thermo-mechanical interplay reproduces the first-order spatiotemporal pattern of deformation and vertical motion across the SCAP, and the characteristic sequence of basin subsidence followed by forearc uplift at a shorter wavelength. This demonstrates that the mechanism of thermally-activated viscous flow, as proposed by Fuller et al. (2006) and expanded here, is an important uplift mechanism that can be applied to the Anatolian margin and potentially be generalized to similar accretionary margins.

2 Background

The Africa/Arabia-Eurasian plate convergence and subduction dynamics that dominate the Mediterranean controls the evolution of the Anatolian margin (Wortel and Spakman, 2000), where the SCAP occupies the forearc high of the Central Cyprus subduction at present (Fig. 1D). Early to Late Miocene subsidence broadened a wide forearc basin that spanned from South Turkey to Central Cyprus, and led to protracted growth of a laterally continuous carbonate platform (e.g., Bassant et al., 2005; Karabıyıkoğlu et al., 2000). Late Miocene regional vertical motions of short wavelength (∼100 km) and opposite sense led to coeval uplift of the forearc high of South Turkey and seaward subsidence (Walsh-Kennedy et al., 2014). These short-wavelength motions of opposite sense fragmented the antecedent forearc basin while forming the SCAP as a flexural monocline absent of regional surface-reaching faults (Fernández-Blanco et al., 2019). The vertical motions led to truncation and erosion of Late Miocene rocks in the uplifting sectors of the SCAP monocline while subsiding sectors sustained deposition (Aksu et al., 2005; Walsh-Kennedy et al., 2014). This leads to latest Messinian-Recent continental sediments with a common Tauride source that have maximum sediment thicknesses of ∼1 km near the Turkish coast and onlap against the Late Miocene erosional contact (Fernández-Blanco et al., 2019). At present, the Late Miocene shallow marine rocks that delineate the monocline lay at ∼2 km elevation in the modern Central Taurides (Cosentino et al., 2012) and at ∼−2 km depth in the Cilicia Basin (Aksu et al., 2005).

Debate persists on when and how the SCAP was formed due to mutually contradictory evidence along the plateau margin (Fig. 1B-1C). An age of 8.35–8.108 Ma is reported for the top of the sequence of marine rocks in the present-day Central Taurides hinterland, now at ~2 km elevation, as constrained by planktonic foraminifera and polarity chrons (Cosentino et al., 2012) (purple star in Fig. 1C). The lateral continuity of these marine rocks across the plateau margin and their contact relationships with the basement, together with the absence of Messinian deposits, suggest km-scale topography by >5 Ma (Fernández-Blanco et al., 2019). This is consistent with stable isotope paleoaltimetry estimates suggesting that ~2 km of relief existed at ~5 Ma (Meijers et al., 2018) (blue circles in Fig. 1B), and with the protracted sedimentary deposition of thick delta lobes stacked in the Göksu Delta (GD in Fig. 1C) since the latest Messinian seen in seismic reflection lines (Aksu et al., 2014; Walsh-Kennedy et al., 2014). Cosmogenic datation in terraces (black squares in Fig. 1C) and uplifted marine fossil assemblages near the Göksu River (GR in Fig. 1C) suggest onset of surface uplift between 8 and 5.45 Ma with average uplift rates of 0.25 to 0.37 mm/yr, and a second uplift phase with rates of 0.72 to 0.74 mm/yr leading to 1.2 km of surface uplift since 1.66 to 1.62 Ma (Schildgen et al., 2012). Paleontological evidence in younger marine rocks at the margins of the Göksu River or closer to the coast (red circles in Fig. 1C), interpreted as 1200-1500 m of topographic growth since ~450 ka, yield uplift rates as fast as 3.21-3.42 mm/yr (Öğretmen et al., 2018). Therefore, ages proposed for the uplift of the Central Taurides range from Late Tortonian to early Middle Pleistocene (~8 Ma; ~5 Ma; ~1.6 Ma; ~0.45 Ma) and are regarded as constraining a single uplift phase at an specific age or several uplift phases, in turn leading to different proposals on the causal mechanisms for SCAP formation.

3 The Anatolian margin

3.1 South Anatolian margin transect: Lithospheric and crustal structure

We reconstruct a plate-scale transect spanning from the East Mediterranean to the Central Anatolian Plateau interior along 33°30'E longitude (Fig. 2). To portray the lithospheric structure, we integrate constraints from Biryol et al. (2011) and Bakırcı et al. (2012) into the TransMED transect VII (Stephenson et al., 2004). To derive the crustal structure and constrain the thicknesses of the African and Anatolian crust as well as the dip of the Cyprus slab, we collectively interpret data from 10+ geophysical studies along the section (Fig. 2B,-C, see caption).

FIG 2 (full page, .ai) - DFB et al.

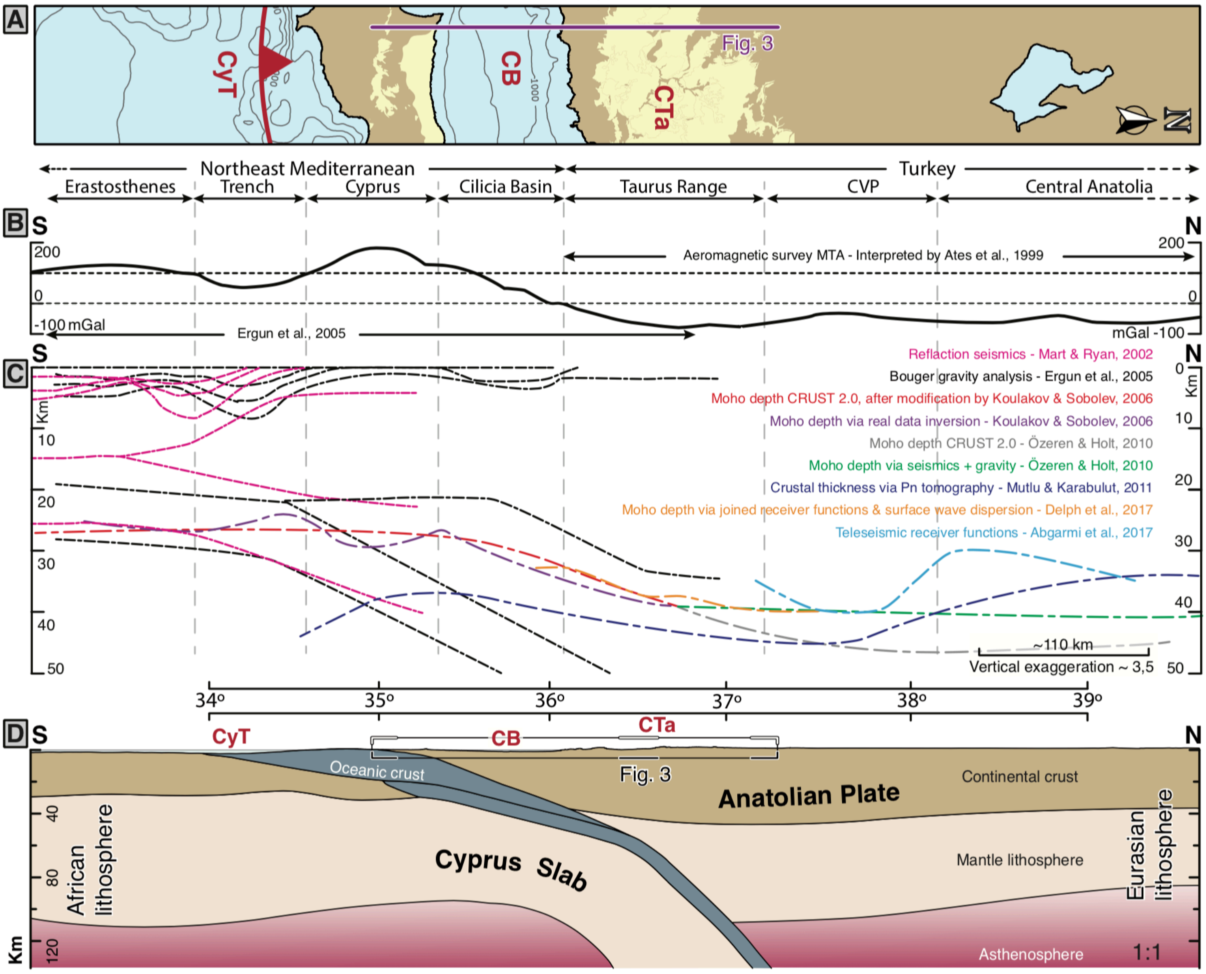

Figure 2. Plate-scale transect along the Anatolian margin in Central Cyrpus. (A) *Map view of a 2°-longitude wide (32°30' E to 34°30' E) swath running ~650 km along latitude, as a reference for data along transects in panels (B) and (C).* ***(B)*** *Values along the section of interest derived from the two major gravimetric studies in the area (Ates et al., 1999; Ergün et al., 2005).* ***(C)*** *Published geophysical data, including the interpretation of the offshore section C in Ergün et al. (2005), and that of the seismic study performed by Mart & Ryan (2002). The cross-section also includes values of depth of the Moho obtained from Moho maps derived by geophysical approaches, including Pn tomography and receiver functions (Abgarmi et al., 2017; Delph et al., 2017; Koulakov and Sobolev, 2006; Mutlu and Karabulut 2011; Özeren and Holt, 2010).* ***(D)*** *Lithospheric-scale transect along the Central Cyprus subduction margin (for ~650 km at 33º30' E) from the interpretation of the data shown in (B) and (C).*

Along the Central Cyprus subduction zone, the African lithosphere under-thrusts northwards below the Anatolian plate (Fig. 2D). The overriding Anatolian lithosphere has maximum thicknesses of ~110 km at the contact with the Cyprus slab below the modern Central Taurides, and thins northwards down to ~85 km in Central Anatolia (Fig. 2D).

In the southern sectors of the transect, crustal thicknesses are recorded by the gravimetric signal of Ergün et al. (2005) and the Moho models of Koulakov and Sobolev (2006). In the African plate, crustal thicknesses of ~28 km are observed at the site of the Eratosthenes Seamount, south of Cyprus, where the African lithosphere is ~40 km thicker than northwards (Fig. 2D). The oceanic crust is the thinnest (~25 km) below the trench area. Northward and between the subducting and overriding plates, thickening occurs in relation to the Troodos Ophiolite, possibly as a result of thrust doubling due to its emplacement. The locked underthrust of the Eratosthenes Seamount is underneath this location, and the detachment depth of the Troodos Ophiolite is uncertain. Similarly, the extent of the continental crust underneath the Troodos Ophiolite and the position of its transition to oceanic crust farther to the north remains enigmatic. The Anatolian plate has a maximum crustal thickness of ~45 km below the Central Taurides (Luccio and Pasyanos, 2007) that decreases gently to ~35 km in the plate interior (Fig. 2D). For this interpretation, we used Pn tomography from Mutlu and Karabulut (2011) instead of gravity data (Özeren and Holt, 2010), which points to crustal thickness values up to 10 km thicker (Fig. 2C).

All geophysical models concur on a northwards increase in Moho depth from ~28 km to >40 km between 34°30'N and 37°N (Fig. 2C) that we correlate with the steepening of the subducting slab (up to 40°) (Fig. 2D). An overall subduction angle of 45° is observed until ~60 km depth at 36°30', where angles of ~60° are reached as the slab deepens. Northward prolongation at similar dips fit appearances of the slab at ~300 km in the interior of Central Anatolia (A-A section of Biryol et al., 2011).

3.2 Central Cyprus forearc transect: Structural and stratigraphic relationships

We reproduce uppermost crustal structures and the geometry of Miocene and younger rocks (Fig. 3) integrating own findings (Fernández-Blanco, 2014; Fernández-Blanco et al., 2019) with published data in regional studies (e.g., Calon et al., 2005; Robertson, 1998a; Stephenson et al., 2004). We assembled the interpretations of each area as shown in their original sources and the reader is referred there for details.

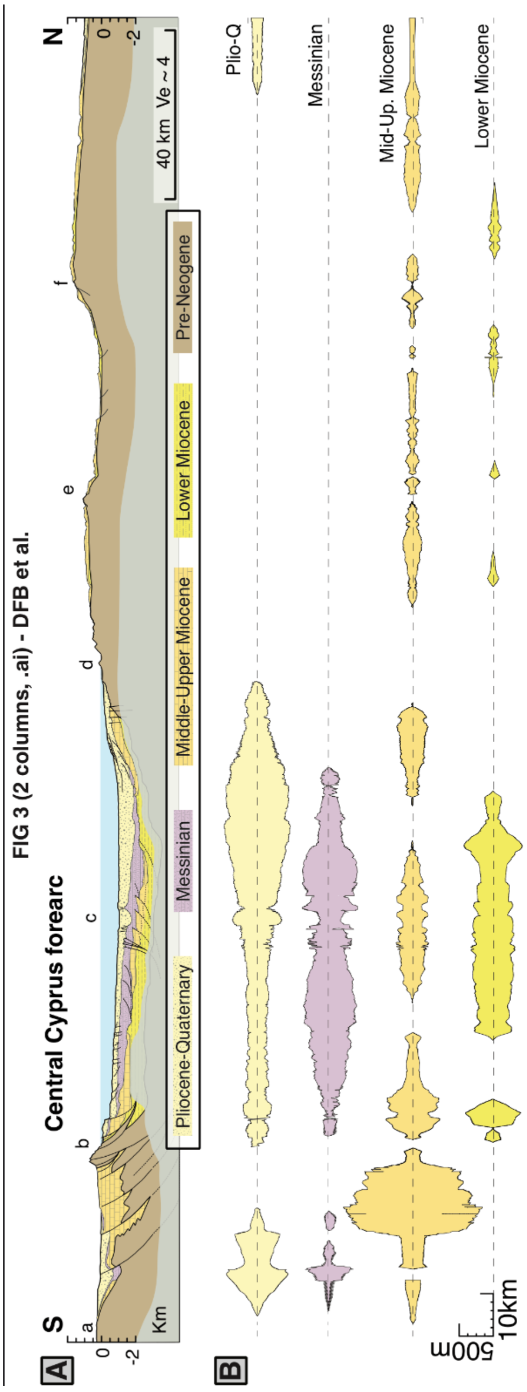

Figure 3. Uppermost crustal transect along the Central Cyprus forearc. ***(A)*** *Geologic transect along the Central Cyprus forearc (for ~300 km at 33º30' E), exaggerated ~4 times in the vertical. Letters "a" to "f" show the approximate location of structural highs bounding basinal sectors with similar lengths. See main text for data used and interpretation.* ***(B)*** *Thicknesses of main stratigraphical units derived from the transect and their age.*

Compressional, regional-scale structures along the Cyprus forearc become older northwards (Fig. 3A). North-dipping thrusts rooted in the subduction megathrust are presently active in the trench and pass northwards into thrust culminations covered by Quaternary and Pleistocene rocks in North Cyprus (Fig. 3A-b). The south-dipping thrust in Central Cilicia Basin is mid-Pliocene (Fig. 3A-c). In the Cilicia Basin northern margin, Messinian salts pinch out where Pliocene rocks overlay an erosional contact with Miocene rocks, attesting to pre-Pliocene uplift. Uplifted Miocene rocks in the Mut Basin delineate a flexural monocline with no Miocene or younger surface-reaching thrusts (Fig. 3A-d). These regional-scale structures result in structural highs that bound basins or basin sectors and compartmentalize the Cyprus forearc at distances of ~40-50 km (Fig. 3A, a to f). A basement high and the Kyrenia Range bound the Messaoria Basin (a to b, ~40 km), and a deep-rooted thrust system in the center of the Cilicia Basin (Fig. 3A-c) set two sub-basins with similar length (~50 km). Basement highs discriminating sectors within the Mut Basin (d, e, f in Fig. 3A) also appear at similar distances. An overriding plate structure with structural highs and lows developing at a constant wavelength from the trench to the forearc high resembles that of accretionary prisms, and is consistent with strain accommodation lead by accretion along the Central Cyprus subduction margin.

Basin infill is regionally continuous until the Messinian and deposited exclusively in seaward sectors of the Central Cyprus forearc thereafter (Fig. 3B). After terrestrial sedimentation, pre-Messinian Miocene neritic limestones were deposited atop pre-Miocene basement (Cosentino et al., 2012). These shallow-water rocks are continuous from the Messaoria Basin, where the pre-Messinian basin thins to the south, to Central Turkey. Since the Messinian, rocks deposited seaward off the present Turkish coast and have basin depocenters occurring at northward locations at younger ages (Fig. 3B). First-order approximations using the minimum and maximum thickness of the youngest unit (Fig. 3B) yield sedimentation rates between ~0.4 mm/yr and ~1.75 mm/yr since the lastest-Messinian. This evidence suggests protracted, large-wavelength subsidence of a wide forearc basin prior to the Messinian, followed by younger surface uplift of the modern Central Taurides with concomitant, counteracting subsidence in the Cilicia Basin.

4 Thermo-mechanical models of accretion

Upper-plate strain and morphology at accretionary margins is often described using the critical wedge theory (e.g., Davis et al., 1983), which defines the geometry of the orogenic wedge as a function of the mechanical properties of the accreting wedge. In its strict, brittle form, the critical Coulomb wedge theory does not include the ductile properties of these systems. Other numerical models able to include more complex rheology and geometry as well as processes such as heat flow and sedimentation have been used to demonstrate deformation patterns at plate margins (e.g., Fillon et al., 2013; Fuller et al., 2006; Mannu et al., 2016; Vanderhaeghe et al., 2003; Willett and Schlunegger, 2010; Williams et al., 1994).

4.1 Model set-up and strategy

We use a 2D kinematic-dynamic model to explore feasible mechanisms leading to the present structure of the Anatolian subduction margin (Fig. 4). The finite element numerical method is used to solve for the mechanical conditions including the geometry and mechanical properties of the accreting material (e.g., Willett, 1992). The model builds from that described in Fuller et al. (2006) and now includes, among other things, sediment deposition through time and strain softening and healing (Cassola, 2013) (see supplementary material). Models are visco-plastic and similar to those in other studies exploring the evolution of accretionary settings over millions of years (e.g., Fillon et al., 2013; Mannu et al., 2016; Vanderhaeghe et al., 2003; Willett and Schlunegger, 2010; Williams et al., 1994). Models simulate the growth of an accretionary wedge at a rate determined by the accretionary flux, as defined by the thickness of accreting material and convergence velocity.

Our simulations aim at being consistent with the time evolution of the Anatolian subduction margin and parameter values are chosen to match plate-scale and upper crustal observations along the transects in Central Cyprus (Figs. 2 & 3) at the end of model run. Models simulate 25

Ma of subduction, with an accretionary thickness h = 3 km and a convergence velocity v_c = 35 mm/yr (Fig. 4), i.e. an accretionary flux of 105 km^2/My. Models have constant accretionary thickness and convergence velocity that are estimates derived from the extrapolation of present-day values over the last 25 Ma and are lower and higher than present, respectively. Present-day sedimentary thicknesses in the East Mediterranean Sea, ranging from 10 km to 15 km (e.g., Makris and Stobbe, 1984), are the largest in the history of the margin, given the narrower confinement of the modern Mediterranean and the presence of the Nile. Similarly, present-day convergence velocities of 9.3 ± 0.3 mm/yr (Reilinger et al., 2006) are slower than in the recent past, possibly due to the underthrusting of the Eratosthenes Seamount below south Cyprus. In general, results scale such that the accretionary flux and run time trade-off at nearly one to one.

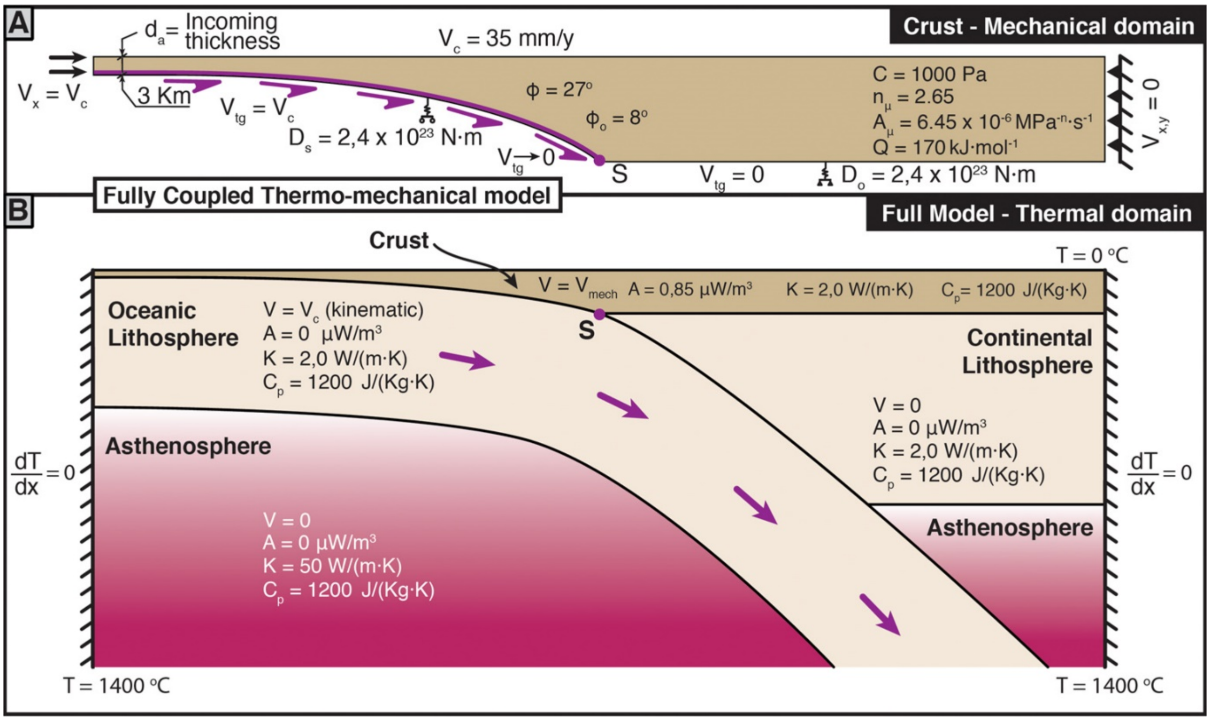

Figure 4. Model setup, with mechanical and thermal parameters. *S is the point of contact between subducting plate and upper plate moho. V is velocity, with* V_c *= convergence velocity;* V_{tg} *= tangential velocity along the base of the mechanical model;* V_x *= velocity in horizontal axis;* V_y *= velocity in vertical axis; and* V_{mech} *= velocity in the mechanical domain, all defined in a reference frame fixed to the undeformed interior of the upper plate.* d_a *is the thickness of incoming sediments.* D_s *and* D_o *are the flexural rigidities of the subducting and overriding plates, respectively. The internal friction angle is represented by* ϕ*, and* ϕ_b *is the friction angle between the subducting and overriding plates. C is cohesion,* A_μ *and* n_μ *are the coefficient and exponent of the power-law viscosity and Q is the activation energy. A is heat production, K is the thermal conductivity, and* C_p *is specific heat. T stands for temperature.*

Models include sediment deposition within closed depressions but sediment source areas are not included, so deposited sediment represents an additional mass flux to the wedge and, ultimately, the crust. Sedimentation in the models fill closed depressions between structural highs. Sediment fill is assumed to be limited by sediment availability, which we parameterize by setting a maximum sedimentation rate. Basins are thus filled only if subsidence is less than this specified sedimentation rate; otherwise basins remain underfilled, with sediment provided at the specified maximum rate. For the parameters and boundary conditions of models shown here, the largest, primary forearc basin is always underfilled and the maximum sedimentation rate defines the effective sedimentation rate throughout most of the basin. Basin peripheral regions and smaller, wedge-top basins may be overfilled, so that sedimentation rates in these regions are less than the specified, maximum rate. Sediments are considered to be continental and have the same material properties as the crust (Fuller et al., 2006). At the time of sedimentation, isochrones are defined as lines on the surface of horizontal sedimentary infill, and subsequently tracked, thereby defining a synthetic stratigraphy of isochronal surfaces at specific time-intervals (2.5 Ma in the main plots and of 1.5 Ma in the insets of Fig. 5). The isostatic load of the sediment is recomputed at every sediment filling step, and displacements added using a flexural model.

The subducting lithosphere is 50 My old at the left side of the model and has a thickness of 70 km that remains constant during the model run. Since thicknesses in the mechanical domain change as material is accreted, we chose an initial thickness of 30 km that leads to end-model crustal thicknesses of 45 km near the "S" point at the plate contact, thereby matching the crustal thickness below the Central Taurides. The rest of the overriding lithosphere is 80 km thick. To let the thermal structure equilibrate, the thermal model runs for 20 My before the crustal model deformation initiates. This matches the known protracted history of subduction in the region and the retreat of the slab near to its present position at 25 Ma (Robertson, 1998b).

Cohesion and internal friction angles control the mechanical strength in our model (Fig. 4, supplementary material). Cohesion, *c*, is set to 1000 Pa, a value somewhat higher than expected for the crust, but this value helps to maintain model stability by preventing gravitational failure of steep surface slopes (Fuller, 2006). The internal friction angle of the crustal material, φ, is set to 27° and the friction angle between the subducting and overriding plate, φ_b, to 8°. Friction values are set low to include the effect of fluid pressures not explicitly taken into account and imply fluid pressure ratios within the range of those at accretionary wedges (Fuller, 2006, and references therein). Isostatic compensation of changing gravitational loads is computed as flexural bending of two broken elastic plates coupled at their common point, which allow whole-model vertical motions in response to sedimentary loading. Other parameter values are not specific to the Anatolian margin nor to our numerical models and are described in detail in Fuller (2006) and Cassola (2013).

4.2 Model results

Model results portray the evolution over millions of years of an accreting subduction wedge, and show the typical morphologic elements of these systems (Fig. 5 & Video S2). Landward of the seaward migrating trench, the trench-slope wedge bounds a wide topographic depression that grows continuously as accommodation space is created by the landward increasing depth of the subduction slab. Steady infill of the forearc depression suppresses deformation of the underlying wedge, providing the stability to maintain an undeformed sedimentary basin in a negative-alpha setting (Fig. 5B). Temperature increases under the basin during its growth leading to a viscosity drop in the lower crust and ductile strain that ultimately results in uplift of the forearc high and subsidence seaward (Fig. 5C). At the conclusion of the model, accretion has led to elevated strain rates and widespread deformation from the trench to the forearc high. Subduction wedge accretion also results in wedge topography and wedge thickness increasing landward up to a crest at the forearc high, where topographic height is maximum.

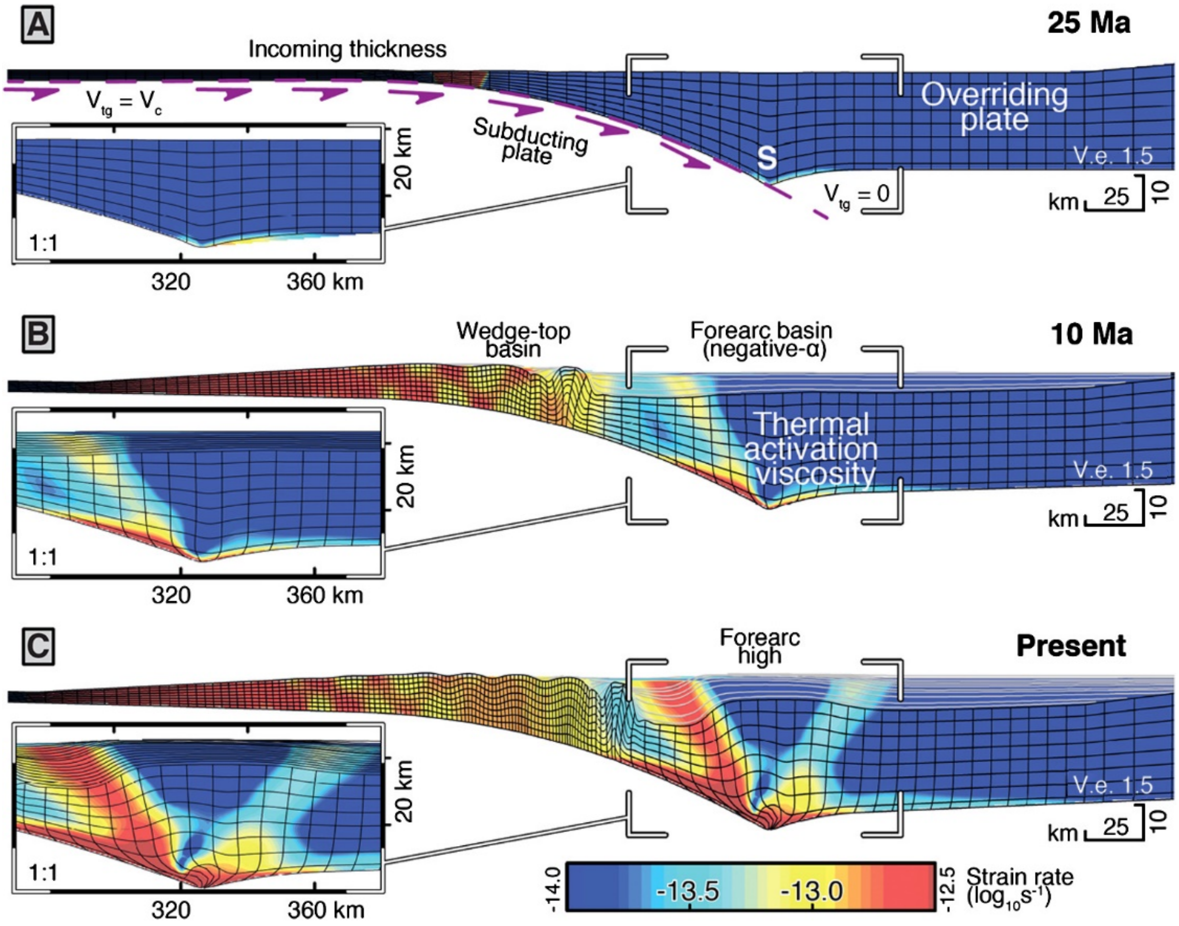

Figure 5. Finite element models of accretion. *Three time-steps (initiation at 25 Ma, 10 Ma and present) in the numerical thermo-mechanical model of viscous-plastic deformation for a convergent wedge undergoing basal traction to simulate subduction. Insets focus on the area where the forearc high develops. The color shows the second invariant of strain rate tensor. The cumulative strain is shown by the Lagrangian mesh. Individual lines on top of the basement are isochrones (synthetic stratigraphy) originally plot horizontal (every 2.5 Ma in the main plots and 1.5 Ma in the insets) and later deformed with the Lagrangian mesh to reflect the overall geometric relationships. The upper panel represents a thermally stable subduction system without prior accretion or deformation. The middle panel at 10 Ma shows a wide forearc (negative-α) basin and a small zone of higher deformation near S point. The bottom panel at present shows a forearc high uplifted by lower crustal flow and two conjugate brittle shear zones. Note the upward of older stratigraphy and syn-tectonic thinning of younger layers over high. The model does not include erosion, so sediments draping the forearc high are still present, but would be expected to erode quickly were this process included. See video Video S2 in Supplementary Material.*

4.2.1 Sedimentation and forearc high uplift

Sedimentation in the forearc basin fundamentally affects vertical motions in the forearc high at advanced stages of wedge evolution. We explore this effect and demonstrate how models with different amounts of sediment fill change the time evolution of relative vertical motion between the highest and lowest points of the forearc basement, i.e the differential between the center of the forearc basin and the top of the forearc high (Fig. 6). At early stages of wedge evolution (15 Ma model run time), variations in maximum sedimentation rate have a minimal effect in forearc topography with relative vertical motions that have constant rates of ~0.04-0.05 mm/yr. Thereafter, sedimentation rates above and below a threshold value result in two different trends in the rate of change of relative vertical motions (Fig. 6, Inset A); whereas lower, below-threshold sedimentation rates (<0.3 mm/yr) lead to convex-up trends in the time evolution of relative vertical displacement, concave-up trends occur with higher, above-threshold sedimentation rates (0.3 mm/yr and higher). Below-threshold sedimentation rates result in rates of relative vertical motion of ~0.2-0.4 mm/yr (black and blue in Fig. 6). Above-threshold sedimentation rates lead to relative vertical motion rates ranging from ~0.72 mm/yr to ~1.75 mm/yr as sedimentation rate changes from 0.3 mm/yr to 1.3 mm/yr, respectively (orange to magenta in Fig. 6).

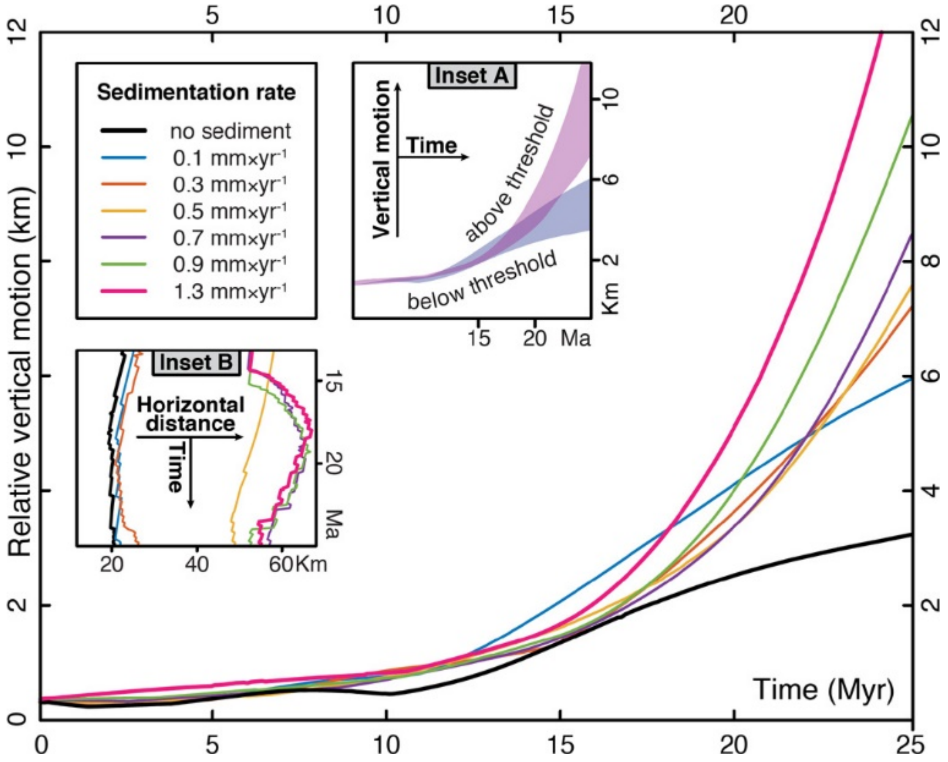

__Figure 6. Sedimentation rate influence on evolution of relative vertical motions in a forearc high.__ Each colored line shows the height difference between the highest and lowest basement elevation in a 100 km strip centered around the S point. Models vary from no sedimentation (black) to a maximum rate of 1.3 mm/yr (magenta). Specified parameter is the maximum permissible sedimentation rate, but given that the basins are underfilled, this rate characterizes the sedimentation rate over most of the basin. Note the nonlinearity in vertical displacement associated with different values of maximum sedimentation rate; for example, the change in vertical motions is roughly the same between 0.7 and 0.9 mm/yr that between 0.9 mm/yr and 1.3 mm/yr, even though sedimentation rate doubles in the latter. Inset A is a schematic representation of vertical motions in time for the groups below and above the threshold in sedimentation rates. Inset B is the evolution in time of the horizontal distance between the highest and the lowest point in the basement surface for the last 12 Ma of model run.

We also track the horizontal distance between the highest and lowest point of the forearc basement during the last stages of model run, i.e. the period of differentiation in vertical motions as led by sedimentation (Fig. 6, Inset B). For all simulations, the horizontal distance between the highest point on the forearc high and the lowest point on its depocenter is short (<70 km) considering the large vertical motion accommodated (up to >12 km). Such horizontal distance is also controlled by the threshold value in sedimentation rate (Fig. 6, Inset B); whereas models with lower sedimentation rates lead to horizontal distances of ~20 km that are consistent throughout the model run, those with higher sedimentation rates show horizontal distances between 40 km and 70 km that vary during the model run. For the latter simulations, once vertical motion initiates, horizontal distances for the tracked points increase suddenly for a period of ~3 Ma and decrease thereon for the rest of the model run (Fig. 6, Inset B). These changes in horizontal distance reflect the steepening in time of the transitional area between uplifting and subsiding areas.

The aforementioned non-linear relation between sedimentation rates and forearc high growth controlled by a threshold value suggests the activation of an external forcing that contributes to vertical motions in the interior of mature wedges. Below, we demonstrate that this is a consequence of forearc basin sedimentation leading to thermally-activated deformation and viscous flow at the base of the crust. This evaluation also provides information on the sensitivity to variations of sedimentation rate regarding this sediment "blanketing" effect.

4.2.2 Sediment blanketing controls on temperature and viscosity

We explore the sedimentation effects on wedge temperature and viscosity. For this, we focus on an area of the mechanical domain centered on the forearc high at the contact between the two plates at moho depth (Fig. 7 and 8A,C). This region is key as it is where the thick upper-plate crust reaches its most seaward point, and thus where the crust is most susceptible to heating and viscous softening as it thickens structurally or is blanketed by sediments. We also evaluate these effects at the base of the crust (Fig. 8B,D).

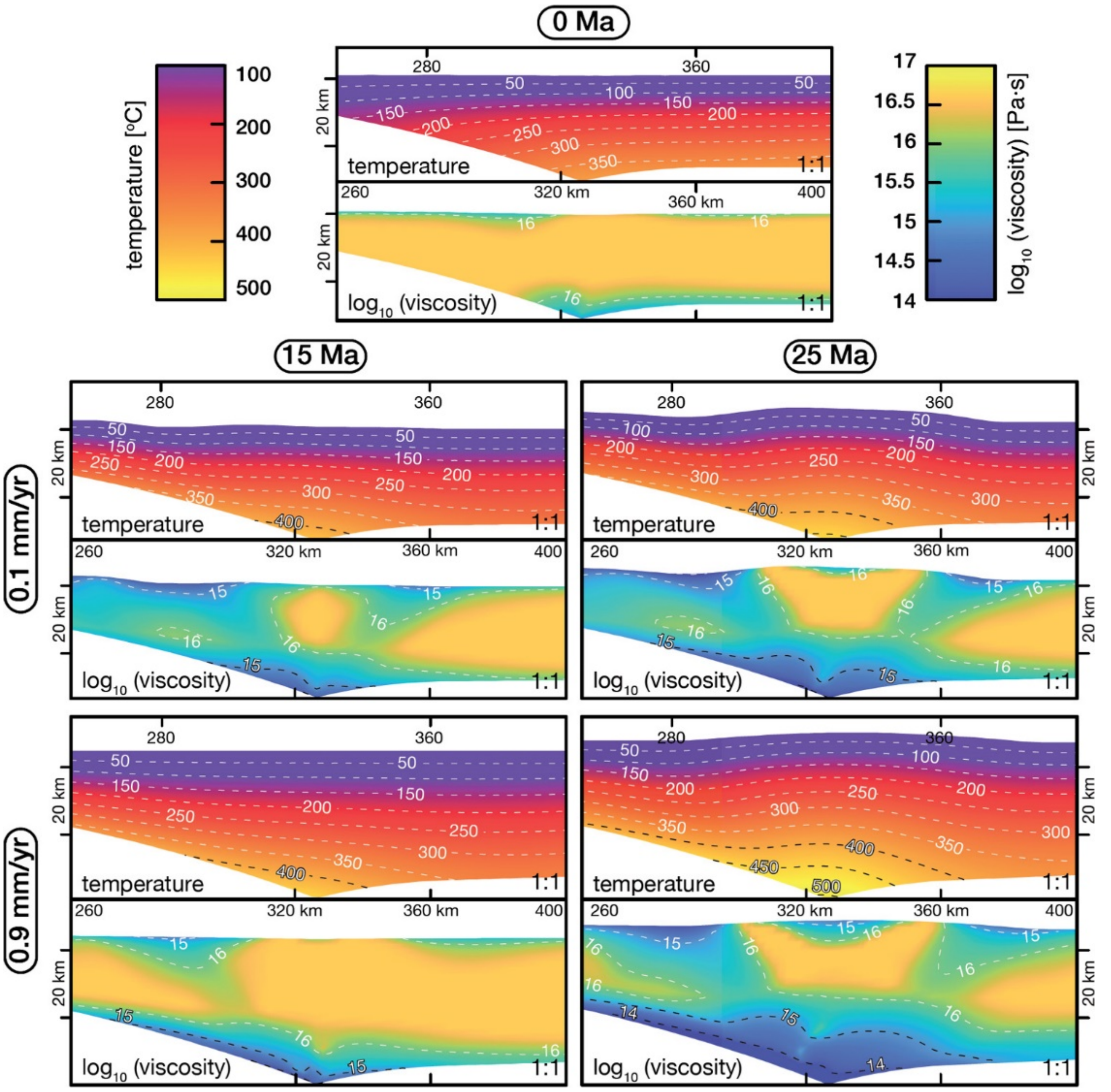

Figure 7. Variations with sedimentation rate in the evolution of the temperature and the viscosity (in logarithmic form) fields. *Pairs of plots of temperature field (top) and viscosity field in logarithmic form (bottom) for model onset (at the top center), 15 Ma (left) and 25 Ma (right). For models at 15 Ma and 25 Ma, maximum sedimentation rates are 0.1 mm/yr in the upper row and 0.9 mm/yr in the bottom row. Plots represent a 140 km wide box of the model mechanical domain centered in the S point. Highlighted in black are specific contours showing the enlarged region of high temperature and low viscosity with increasing sedimentation fill level.*

Figure 8. Temperature and viscosity variation of the forearc high and crustal base with sediment fill level. *Evolution of median ($\hat{x}$) temperature and median ($\hat{x}$) viscosity in the forearc high region (A; C) and base of the crust (B; D). Areas considered are centered in the S point; 140 km wide x 45 km tall for the forearc high region and 200 km wide x 20 km tall for the base of the crust. We assure a representative, non-parametric calculus, we use the median for both temperature field and viscosity distribution. For the former, we compute median temperature values for each grid point, thereby avoiding potential complications related to multi-modal distributions in temperature fields of geodynamic models. For the latter, we compute the median viscosity of highly-strained regions. To avoid the tendency of average values to misrepresent power-law distributions, we calculate the strain rates for all grid elements and use the median viscosity of the 10% with larger strain rates. Different line colors represent the maximum sedimentation rates of 0.1 mm/yr (blue), 0.3 mm/yr (red), 0.5 mm/yr (yellow), 0.7 mm/yr (purple), and 0.9 mm/yr (green). Note the decrease in crustal viscosity due to crustal thickening, with sedimentation increasing the effect.*

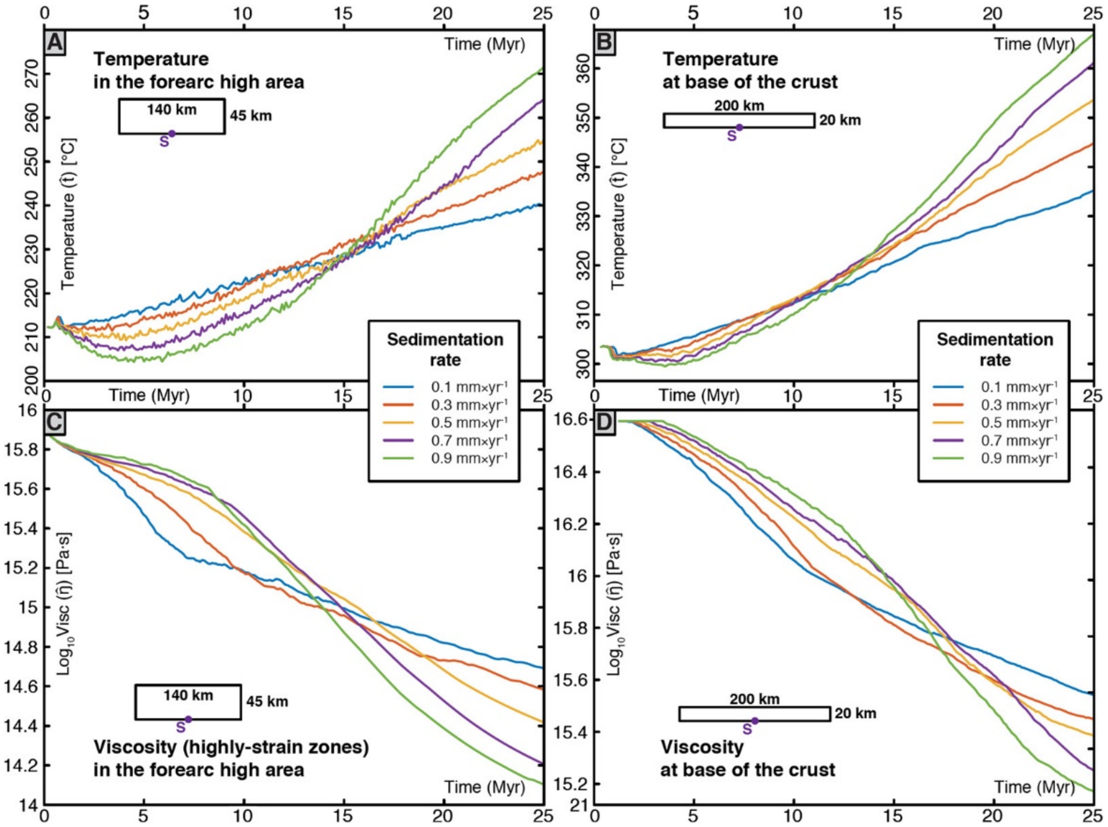

We plot the temperature and viscosity fields in this designated forearc region for models before onset, at 15 Ma and 25 Ma for sedimentation rates of 0.1 mm/yr and 0.9 mm/yr (Fig. 7). Models show increased temperature and decreased log(viscosity) values for older models and models with larger sedimentation rates. Areas of higher temperatures and lower viscosities at the base of the crust (marked as black contours in Fig. 7) are enlarged along the base of the crust and upwards for the case with increased sedimentation fill level, especially for the 25 Ma case.

We plot a characteristic metric of the median temperature (Fig. 8A) and median viscosity (Fig. 8B) within this designated forearc region for models with sedimentation rates ranging from 0.1 mm/yr to 0.9 mm/yr. These plots prove that the increase in strain rate within this region shown by the models (Fig. 5, Video S2) is directly a consequence of the increase in temperature and the subsequent decrease in viscosity (Fig. 8). Deformation in the lower crust is temperature-dependent and thus dominated by viscous flow, rather than brittle, plastic deformation.

The thickness of the wedge-top sediments determine the total temperature drop or "blanketing" of the underlying crust and thereby its viscosity (Fig. 7 and 8). There is an interesting second effect in the first 15 Ma of the models. Initially, the median temperature decreases in response to the deposition of cold sediment, but as these sediments heat so does the underlying crust, ultimately leading to a long-term signal of heating and viscous softening. Models reveal a transition at ~15 Ma, when the same wedge temperature is recorded for all models, regardless of their sedimentation rate (Fig. 8), reflecting the timescale for heat diffusion from the lower crust to the surface. The evolution of viscosity, both in the forearc high area and at the base of the crust, show a similar transition with increased sedimentation rates (Fig. 8C,D). Both sedimentation cooling and conductive crustal heating scale with sedimentation rate and total sediment deposited, as shown by the models in which sedimentation rate varies from 0.1 mm/yr to 0.9 mm/yr (Fig. 8).

These models show that sedimentation can play an important role in the growth of a forearc high in mature accretionary wedges, and the rate of associated topographic growth, ultimately leading to vertical motions of opposite sense and short wavelength (Fig. 6). The relationship between sedimentation rate and larger relative vertical motions in the forearc high through the relationship with temperature and viscosity (Fig. 8) demonstrate the viability of a mechanical model in which sediments have a "thermal blanketing" effect that induces viscous flow in the lower crust and the uplift of the forearc high. Thermal resistivitance of sediments leads to higher temperatures directly below the forearc basin as it grows (Fig. 7), and ultimately results in high strain rate viscous flow at the base of the crust (Figs. 5B & 7). Given the compressional state of the wedge and upper plate crust, the forearc shortens horizontally and thickens, uplifting the forearc high (Fig. 5C). Thus, the forearc basin "thermal blanket" promotes deep-seated deformation that, in the context of accretion, propels the uplift of the forearc high while subsidence continues in seaward regions that are unaffected by viscous softening and flow (Figs. 5 to 8).

5 Discussion

Deep-seated flow (Pavlis and Bruhn, 1983) at the base of an orogenic wedge (Platt, 1986; Willett et al., 1993) provides a simple general framework to explain the dynamic formation of forearc highs. Crustal thickening by protracted wedge accretion increases the depth of burial and the temperature of the lower crust (Willett et al., 1993). Synorogenic sedimentation filling of a forearc basin similarly contributes to wedge thickening, and also raises lower crustal temperatures by increasing thermal resistance and, if sediment conductivity is low, the geothermal gradient through the basin (Fuller et al., 2006).

5.1 Dynamic growth of forearc highs

The fundamental conditions required by the model presented here are quite simple. Accretion and syn-accretion sedimentation result in a progressive increase of crustal thickness in a subduction margin forearc. The increased thickness increases thermal resistance and Moho depth, thereby increasing lower crustal temperatures and thermally triggering viscous flow at significant strain rates. Under protracted accretion and shortening, ductile strain in the lower crust switches vertical tectonic motions in the overlying wedge, from forearc basin subsidence to uplift, forming a new forearc high directly under the former basin (Fig. 9). We expect this process to take place in any accretionary system as it matures and increases in size, as for example documented on the Cascadia margin (Fuller et al., 2006; McNeill et al., 2000).

A forearc high located in the wedge rear and controlled by viscous flow, as we propose here, will form at a location determined by the geometry of the slab as an integral part of accretionary wedges. In this context, forearc highs become more probable as the accretion system matures, eventually uplifting the wedge rear in a dynamic, non-linear manner at a time dictated by accretionary flux, wedge temperature, and wedge viscosity. We note, however, that there are other mechanisms for the formation of a forearc high, including forced mechanical accretion against areas of relatively larger strength (Byrne et al., 1993), changes in wedge taper or stress state, or other processes leading to deep-seated ductility (Pavlis and Bruhn, 1983), such as the presence of fluids.

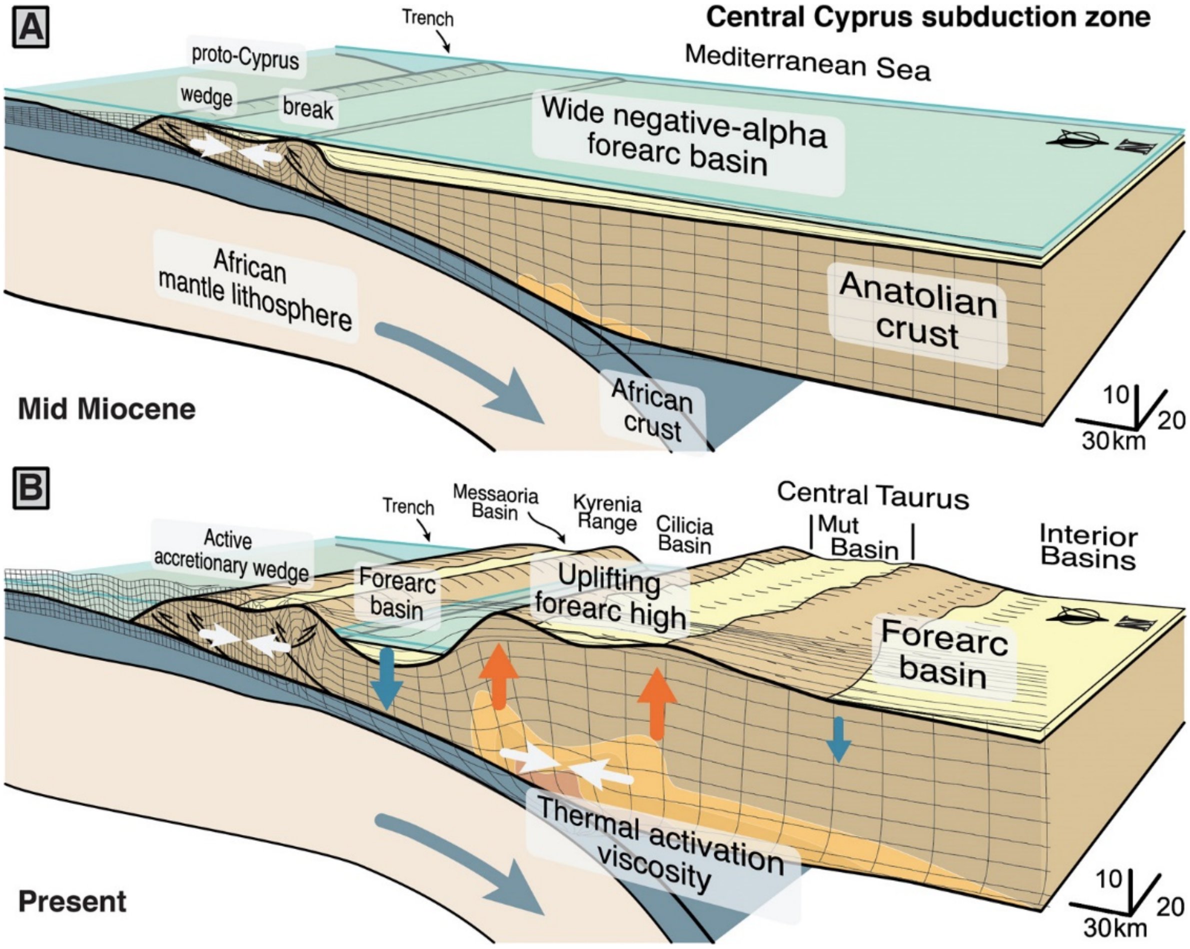

Figure 9. Mechanism of thermo-viscous uplift. *Box model representation of the mechanism of thermo-viscous forearc high uplift in two time-steps. Boxes show the evolution and forearc elements for a generic subduction wedge with forearc high and for the Central Cyprus margin. Time steps are interpreted as representative of the Central Cyprus margin. Integrated deformation is shown using the Lagrangian mesh of the model. Note that the model is only two-dimensional.*

Competing, dynamic effects control the uplift of the forearc high. Synorogenic sedimentation increases the thermal resistance and thus the temperature of the underlying crust. This effect would be even more pronounced should sediments have had a lower thermal conductivity than the rest of the crust, which is not the case in our models. While a weaker lower crust tends to decrease the wedge taper, it also facilitates ductile strain that, when sustained by accretion, results in increasing the wedge taper. Therefore, the taper geometry of the internal sectors of the wedge depends not only on convergence velocity (Willett et al., 1993) but also on its interplay with forearc basin sedimentation. The area undergoing lower crustal flow generates uplift in regions immediately above it, while trenchward regions not affected by lower crustal flow continue to subside through sediment loading. The transitional area from forearc high to trenchward subsidence is regarded as ductile-to-frictional decollement in Williams et al., (1994).

Sedimentation controls the lag time between wedge growth and thermal activation of lower crustal flow. Whereas no topographic growth occurs in the internal sectors of the wedge during its early evolution, regardless of the amount of sediments in the forearc, a threshold in the amount of sediment in the forearc controls the growth of the forearc high at advanced stages of wedge (Figs. 6 to 9). This implies that the lower crustal flow is controlled by the thickness of the crust, which depends in turn on the sedimentation rates in the forearc basin. In other words, the sedimentary blanketing effect controls the lower crustal flow in so that the drop in viscosity does not occur until sediment thickness reaches a threshold. Otherwise, crustal thickening alone would eventually lead to viscous deformation, albeit occurring later and possibly elsewhere in the mechanical system. Therefore, an increasingly fast rate of vertical motions, a short horizontal distance between uplifting and subsiding terrains, and their location above the contact point between overriding crust and slab, all are diagnostic of the sedimentary blanketing effect leading to viscous uplift of the forearc high.

Sedimentation and sedimentation rate have other effects that control forearc high uplift. Sediment infill of the forearc topographic depression reduces the surface angle of the forearc wedge to zero and stabilizes the wedge underneath, resulting in a broad wedge where active deformation is confined to an outer wedge removed from any material-controlled backstop (Fuller et al., 2006). In addition, isostatic basin subsidence by sediment loading of the forearc persists seaward and landward of the uplifting forearc high. This leads to the apparent paradox that regional subsidence in the forearc basin can control uplift in the forearc high for cases where sedimentation rate outpaces accommodation space, i.e. when subsidence controls the amount of sediment entering the system.

5.2 Growth of the Anatolian margin

Our simulations are consistent with SCAP formation as a dynamic, thermo-viscous forearc high led by forearc sedimentation and accretion along Central Cyprus (Fig. 9). Models reproduce the growth of the SCAP, including the surface uplift of Central Taurus and coeval subsidence in the Cilicia Basin, resulting in the monoclinal flexure of Late Miocene rocks at plateau margin scale (Fernández-Blanco et al., 2019) (Figs. 3 & 9). This is compatible with surface uplift onset between 8 and 5.45 Ma in the plateau margin hinterland (Cosentino et al., 2012), and a well-developed orogenic rain shadow by 5 Ma (Meijers et al., 2018) as well as the concomitant, short-wavelength vertical tectonic motions described for S Turkey (Fernández-Blanco et al., 2019; Walsh-Kennedy et al., 2014). Models are also consistent with observational evidence like the undisrupted sedimentary record in the SCAP offshore through latest Messinian - Recent times (Aksu et al., 2014, 2005; Walsh-Kennedy et al., 2014). Therefore, the mechanism of dynamic, thermo-viscous forearc high growth provides a physical support for models of SCAP growth by contraction and crustal thickening (Fernández-Blanco, 2014; Fernández-Blanco et al., 2019; Meijers et al., 2018).

Accelerated uplift rates during the uplift of the Central Taurides forearc can be inferred from the elevations of Miocene to Pleistocene marine rocks. These rocks show that the onset of uplift initiated at ~8 Ma (Cosentino et al., 2012) and accelerated to ~0.75 mm/yr over the last ~1.6 Ma (Schildgen et al., 2012). Our models show the occurrence of an equivalent accelerated uplift as a natural consequence of the non-linear uplift associated with thermal weakening of the lower crust (Fig. 5B,-C, 6, 7, 8, 9B). Most observations of uplift rates are consistent with our models, but one study has suggested that 1200-1500 m of topographic growth occurred within the last ~450 ka (Öğretmen et al., 2018). The spatial location of the marine deposits analysed by this study is relatively local, but if applicable to the entire margin, it would be difficult to reconcile with our models.

Schildgen et al. (2012) argued that uplift rates exhibited a rapid increase in rate initiating at about ~1.6 Ma, on the basis of analysis of knickpoints in rivers draining the Central Taurides.

However, the river knickpoints are not particularly uniform in their elevation or along-channel distribution, and could be consistent with a gradual increase in uplift rate from Late Miocene to the present, particularly if other complicating factors such as tilting and river capture are taken into account. Similarly, these studies interpret the depositional age or subaerial exposure of marine rocks at individual sites in terms of uplift age and uplift spatiotemporal pattern, i.e. temporal phases of uplift at margin scale. However, the uplifted marine sediment data cannot resolve sharp changes in uplift rate and only show that rates averaged over the Pliocene and Late Miocene were lower than rates over the Pleistocene to modern.

Primary alternative models for uplift of the Taurides forearc high suggest shallow slab break-off and multiple-phase surface uplift (e.g., Schildgen et al., 2014). However, slab break-off models do not inherently predict extended periods of uplift or accelerated uplift, so the earlier uplift during the Miocene has been attributed to structural thickening, similar to what we predict here (Schildgen et al., 2014) with the high rates of uplift associated with slab break-off in the last ~1.6 Ma (Schildgen et al., 2012) or younger times (Öğretmen et al., 2018). Slab break-off is an independent process to lower crustal viscous flow and it is possible that both have occurred and contribute to the uplift of S Turkey. However, our models show that there are combinations of parameters that predict growth rates, timing and accelerations consistent with the observations, with no need for slab break-off as a second process.

Our models show that compression-driven wedge growth with sedimentation can not only provide an uplift mechanism for the southern margin of the Central Anatolian Plateau but also reproduce first-order upper plate strain and the complex geometry and patterns of vertical motion in space and time that characterize the southern Anatolian margin (Figs. 3 & 9). These simulations agree with the regional frame and the geological and geophysical observables in the Anatolian margin along the Central Cyprus subduction zone, including on and under the area undergoing maximum uplift. The Kyrenia Range trench-slope break divides the active frictional deformation in the seaward areas, resulting in formation of the wedge-top basin of Messaoria, distinct from the negative-alpha Cilicia Basin, and from areas farther landward where thermally-activated viscosity in the deeper sectors of the wedge resulted in the uplift of the modern Central Taurides (Figs. 3, 5 & 9). Our simulations are valid for the central sector of the Cyprus subduction zone only (approximately delimited by Fig. 2A), given the notable lateral variability along the Cyprus margin. Similarly, although our simulations could reproduce the dynamic growth of wider plateau-like terrains, the mechanism presented here cannot be responsible for the topography of the entire Central Anatolian Plateau, given the thin crust in the plateau interior (e.g., Abgarmi et al., 2017). This mechanism is also compatible with disruption of the former forearc basin by uplift of the forearc high in Cascadia (McNeill et al., 2000), and suggests similar processes in margins with long-lived sedimentation and large amounts of accreted material, like the Lesser Antilles, the Alaskan and the Makran accretionary complexes (Pavlis and Bruhn, 1983).

6 Conclusions

Integration and interpretation of geophysical and geological evidence along the Anatolian subduction margin from the Central Cyprus trench to the SCAP suggests that lithospheric and crustal thicknesses, as well as Miocene and younger regional-scale structures and derived tectono-stratigraphic features formed by accretionary subduction. In this context, thermally-activated viscous flow of the lower crust is a physical mechanism of forearc high growth. Thermo-mechanical models of this process show that this single mechanism can explain much of the complex space and time pattern of vertical motions in the Anatolian subduction margin, with no need for an additional mechanism such as slab breakoff. We conclude that the plateau margin in South Turkey, and areas with a similar sequence of vertical motions in the interior of other accreting subduction wedges, grow as dynamic, thermo-viscous forearc highs.

Acknowledgments

The authors want to thank three anonymous reviewers for their constructive criticisms. We thank the Netherlands Organisation for Scientific Research (NWO) for founding this study as a part of the Vertical Anatolian Movement Project (VAMP), an European Science Foundation (ESF) EuroCORE project within TOPOEurope. Grant/Award Number: 855.01.142 (07-TOPO-EUROPE-FP-013) Miocene tectonics in the Central Anatolia Plateau, and the Netherlands Organisation for Scientific Research. DFB thanks Teodoro Cassola for his guidance with the models, and Melodie Philippon and Christoph von Hagke for discussions on early versions of the manuscript.

References

Abgarmi, B., Delph, J.R., Arda Ozacar, A., Beck, S.L., Zandt, G., Sandvol, E., Turkelli, N., Berk Biryol, C., 2017. Structure of the crust and African slab beneath the central Anatolian plateau from receiver functions: New insights on isostatic compensation and slab dynamics. Geosphere 13, 1774–1787.

Aksu, A.E., Calon, T.J., Hall, J., Mansfield, S., Yaşar, D., 2005. The Cilicia–Adana basin complex, Eastern Mediterranean: Neogene evolution of an active fore-arc basin in an obliquely convergent margin. Marine Geology 221, 121–159.

Aksu, A.E., Walsh-Kennedy, S., Hall, J., Hiscott, R.N., Yaltırak, C., Akhun, S.D., Çifçi, G., 2014. The Pliocene–Quaternary tectonic evolution of the Cilicia and Adana basins, eastern Mediterranean: Special reference to the development of the Kozan Fault zone. Tectonophysics 622, 22–43.

Allmendinger, R., Jordan, T., Kay, S., Isacks, B., 1997. The evolution of the Altiplano-Puna plateau of the Central Andes. Annual Review of Earth and Planetary Sciences 25, 139–174.

Ates, A., Kearey, P., Tufan, S., 1999. New gravity and magnetic anomaly maps of Turkey. Geophys. J. Int. 136, 499–502.

Bakırcı, T., Yoshizawa, K., Özer, M., 2012. Three-dimensional S-wave structure of the upper mantle beneath Turkey from surface wave tomography. Geophysical Journal International 190, 1058–1076.

Bartol, J., Govers, R., 2014. A single cause for uplift of the Central and Eastern Anatolian plateau? Tectonophysics 637, 116–136.

Bassant, P., Van Buchem, F.S.P., Strasser, A., Görür, N., 2005. The stratigraphic architecture and evolution of the Burdigalian carbonate—siliciclastic sedimentary systems of the Mut Basin, Turkey. Sedimentary Geology 173, 187–232.

Biryol, C., Beck, S.L., Zandt, G., Özacar, A., 2011. Segmented African lithosphere beneath the Anatolian region inferred from teleseismic P-wave tomography. Geophysical Journal International 184, 1037–1057.

Byrne, D.E., Wang, W.-H., Davis, D.M., 1993. Mechanical role of backstops in the growth of forearcs. Tectonics 12, 123–144.

Calon, T.J., Aksu, A.E., Hall, J., 2005. The Oligocene-Recent evolution of the Mesaoria Basin (Cyprus) and its western marine extension, Eastern Mediterranean. Marine Geology 221, 95–120.

Cassola, T., 2013. Mechanics of forearc basins. ETH Zurich.

Cosentino, D., Schildgen, T., Cipollari, P., Faranda, C., Gliozzi, E., Hudáčková, N., Lucifora, S., Strecker, M.R., 2012. Late Miocene surface uplift of the southern margin of the Central Anatolian Plateau, Central Taurides, Turkey. Geological Society of America Bulletin 124, 133–145.

Davis, D., Suppe, J., Dahlen, F.A., 1983. Mechanics of fold-and-thrust belts and accretionary wedges. Journal of Geophysical Research.

Delph, J.R., Abgarmi, B., Ward, K.M., Beck, S.L., Arda Özacar, A., Zandt, G., Sandvol, E., Türkelli, N., Kalafat, D., 2017. The effects of subduction termination on the continental lithosphere: Linking volcanism, deformation, surface uplift, and slab tearing in central Anatolia. Geosphere 13, 1788–1805.

Ergün, M., Okay, S., Sari, C., Zafer Oral, E., Ash, M., Hall, J., Miller, H., 2005. Gravity anomalies of the Cyprus Arc and their tectonic implications. Marine Geology 221, 349–358.

Fernández-Blanco, D., 2014. Evolution of Orogenic Plateaus at Subduction Zones: Sinking and raising the southern margin of the Central Anatolian Plateau. Amsterdam Vrije Universiteit.

Fernández-Blanco, D., Bertotti, G., Aksu, A., Hall, J., 2019. Monoclinal flexure of an orogenic plateau margin during subduction, south Turkey. Basin Research 13, 1774.

Fillon, C., Huismans, R.S., van der Beek, P., 2013. Syntectonic sedimentation effects on the growth of fold-and-thrust belts. Geology 41, 83–86.

Fuller, C.W., 2006. Controls on the Structural Morphology and Subduction-thrust Seismicity of Accretionary Margins. University of Washington.

Fuller, C.W., Willett, S.D., Brandon, M.T., 2006. Formation of forearc basins and their influence on subduction zone earthquakes. Geology 34, 65–68.

Göğüş, O.H., Pysklywec, R.N., Şengör, A.M.C., Gün, E., 2017. Drip tectonics and the enigmatic uplift of the Central Anatolian Plateau. Nature Communications 8, 1538.

Karabıyıkoğlu, M., Çiner, A., Monod, O., Deynoux, M., Tuzcu, S., and Örçen, S., 2000. Tectonosedimentary evolution of the Miocene Manavgat Basin, western Taurides, Turkey. Geological Society, London, Special Publications 137, 271–294.

Koulakov, I., Sobolev, S.V., 2006. Moho depth and three-dimensional P and S structure of the crust and uppermost mantle in the Eastern Mediterranean and Middle East derived from tomographic inversion of local ISC data. Geophys. J. Int. 164, 218–235.

Luccio, F., Pasyanos, M.E., 2007. Crustal and upper-mantle structure in the Eastern Mediterranean from the analysis of surface wave dispersion curves. Geophys. J. Int. 169, 1139–1152.

Makris, J., Stobbe, C., 1984. Physical properties and state of the crust and upper mantle of the Eastern Mediterranean Sea deduced from geophysical data. Marine Geology 55, 347–363.

Mannu, U., Ueda, K., Willett, S.D., Gerya, T.V., Strasser, M., 2016. Impact of sedimentation on evolution of accretionary wedges: Insights from high-resolution thermomechanical modeling. Tectonics 35, 2016TC004239.

Mart, Y., Ryan, W.B.F., 2002. The complex tectonic regime of Cyprus arc: a short review. Isr. J. Earth Sci. 51, 117–134.

McNeill, L.C., Goldfinger, C., Kulm, L.D., Yeats, R.S., 2000. Tectonics of the Neogene Cascadia forearc basin: Investigations of a deformed late Miocene unconformity. GSA Bulletin 112, 1209–1224.

Meijers, M.J.M., Brocard, G.Y., Cosca, M.A., Lüdecke, T., Teyssier, C., Whitney, D.L., Mulch, A., 2018. Rapid late Miocene surface uplift of the Central Anatolian Plateau margin. Earth and Planetary Science Letters 497, 29–41.

Molnar, P., 1984. Structure and Tectonics of the Himalaya: Constraints and Implications of Geophysical Data. Annual Review of Earth and Planetary Sciences 12, 489–516.

Mutlu, A.K., Karabulut, H., 2011. Anisotropic Pn tomography of Turkey and adjacent regions. Geophys. J. Int. 187, 1743–1758.

Öğretmen, N., Cipollari, P., Frezza, V., Faranda, C., Karanika, K., Gliozzi, E., Radeff, G., Cosentino, D., 2018. Evidence for 1.5 km of uplift of the Central Anatolian Plateau's southern margin in the last 450 kyr and implications for its multi-phased uplift history. Tectonics 2017TC004805.

Özeren, M.S., Holt, W.E., 2010. The dynamics of the eastern Mediterranean and eastern Turkey. Geophys. J. Int. 183, 1165–1184.

Pavlis, T.L., Bruhn, R.L., 1983. Deep-seated flow as a mechanism for the uplift of broad forearc ridges and its role in the exposure of high P/T metamorphic terranes. Tectonics 2, 473–497.

Platt, J.P., 1986. Dynamics of orogenic wedges and the uplift of high-pressure metamorphic rocks. GSA Bulletin 97, 1037–1053.

Reilinger, R., McClusky, S., Vernant, P., Lawrence, S., Ergintav, S., Cakmak, R., Ozener, H., Kadirov, F., Guliev, I., Stepanyan, R., Nadariya, M., Hahubia, G., Mahmoud, S., Sakr, K., ArRajehi, A., Paradissis, D., Al-Aydrus, A., Prilepin, M., Guseva, T., Evren, E., Dmitrotsa, A., Filikov, S.V., Gomez, F., Al-Ghazzi, R., Karam, G., 2006. GPS constraints on continental deformation in the Africa-Arabia-Eurasia continental collision zone and implications for the dynamics of plate interactions: Eastern Mediterranean active tectonics. Journal of Geophysical Research, Geodyn. Ser. 111. https://doi.org/10.1029/2005JB004051

Robertson, A.H.F., 1998a. Mesozoic-Tertiary tectonic evolution of the easternmost Mediterranean area: integration of marine and land evidence. Proceedings of the Ocean Drilling Program, Scientific Results, Vol. 160; Chapter 54.

Robertson, A.H.F., 1998b. Tectonic significance of the Eratosthenes Seamount: a continental fragment in the process of collision with a subduction zone in the eastern Mediterranean (Ocean Drilling Program Leg 160). Tectonophysics 298, 63–82.

Schildgen, T.F., Cosentino, D., Bookhagen, B., Niedermann, S., Yıldırım, C., Echtler, H., Wittmann, H., Strecker, M.R., 2012. Multi-phased uplift of the southern margin of the Central Anatolian plateau, Turkey: A record of tectonic and upper mantle processes. Earth and Planetary Science Letters 317–318, 85–95.

Schildgen, T.F., Yıldırım, C., Cosentino, D., Strecker, M.R., 2014. Linking slab break-off, Hellenic trench retreat, and uplift of the Central and Eastern Anatolian plateaus. Earth-Science Reviews 128, 147–168.

Stephenson, R.A., Mart, Y., Okay, A., Robertson, A., Saintot, A., Stovba, S., Khriachtchevskaia, O., 2004. TRANSMED Transect VIII: Eastern European Craton--Crimea--Black Sea--Anatolia--Cyprus--Levant Sea--Sinai--Red Sea. The TRANSMED Atlas: The Mediterranean Region from Crust to Mantle 120–127.

Vanderhaeghe, O., Medvedev, S., Fullsack, P., Beaumont, C., Jamieson, R.A., 2003. Evolution of orogenic wedges and continental plateaux: insights from crustal thermal–mechanical models overlying subducting mantle lithosphere. Geophys. J. Int. 153, 27–51.

Walsh-Kennedy, S., Aksu, A.E., Hall, J., Hiscott, R.N., Yaltırak, C., Çifçi, G., 2014. Source to sink: The development of the latest Messinian to Pliocene–Quaternary Cilicia and Adana Basins and their linkages with the onland Mut Basin, eastern Mediterranean. Tectonophysics 622, 1–21.

Willett, S., Beaumont, C., Fullsack, P., 1993. Mechanical model for the tectonics of doubly vergent

compressional orogens. Geology 21, 371–374.
Willett, S.D., 1992. Dynamic and kinematic growth and change of a Coulomb wedge, in: McClay, K.R. (Ed.), Thrust Tectonics. Springer Netherlands, Dordrecht, pp. 19–31.
Willett, S.D., Schlunegger, F., 2010. The last phase of deposition in the Swiss Molasse Basin: from foredeep to negative-alpha basin. Basin Research 22, 623–639.
Williams, C.A., Connors, C., Dahlen, F.A., Price, E.J., Suppe, J., 1994. Effect of the Brittle-Ductile Transition on the Topography of Compressive Mountain Belts on Earth and Venus. Journal of Geophysical Research-Solid Earth 99, 19947–19974.
Wortel, M., Spakman, W., 2000. Subduction and slab detachment in the Mediterranean-Carpathian region. Science 290, 1910–1917.
Yildirim, C., Schildgen, T.F., Echtler, H., Melnick, D., Strecker, M.R., 2011. Late Neogene and active orogenic uplift in the Central Pontides associated with the North Anatolian Fault: Implications for the northern margin of the Central Anatolian Plateau, Turkey. Tectonics 30, TC5005.

Supplementary Material for

Forearc high uplift by lower crustal flow during growth of the Cyprus-Anatolian margin

David Fernández-Blanco[1,*], Utsav Mannu[2,3], Giovanni Bertotti[4], and Sean D. Willett[1]

[1] Geological Institute, Swiss Federal Institute of Technology, 8092 Zurich, Switzerland.
geo.david.fernandez@gmail.com
[2] Earthquake and Volcano Information, Earthquake Research Institute, Tokyo University.
[3] Department of Earth & Climate, Indian Institute of Science Education and Research, Pune.
[4] Department of Geoscience and Engineering, Faculty of Civil Engineering and Geosciences, Delft University of Technology.
** Now at: Consejo Superior de Investigaciones Científicas (CSIC), Instituto de Ciencias del Mar (ICM), Passeig Marítim de la Barceloneta, 37-49, E-08003 Barcelona, Spain*

Contents of the Supplementary Material (caption)

This supplement contains Supplementary Text, detailing the numerical code used; Figure S1, showing the Arbitrary Lagrangian-Eulerian and thermal meshs used in the models; Video S2, that shows our preferred model; and Table S3, showing the mechanical and thermal parameters used in the models.

Introduction

Accretionary wedges at convergent margins and their associated forearc systems are mechanically analogous to a wedge of sand piled upfront a bulldozer, where the behavior of the taper angle between the surface slope and the basal dip is described by the critical wedge theory (e.g., Davis et al., 1983; Dahlen, 1984; Willett, 1992; Wang and Davis, 1996). For a given set of wedge mechanical properties (internal friction angle, basal friction, pore fluid pressure, cohesion), the taper angle is constant and the wedge grows self-similarly as new sediments accrete at its toe (e.g., Dahlen, 1984). If the taper angle becomes larger than critical, the wedge attains stability by displacing deformation toe-wards (sea-wards) whereas if the taper angle is smaller than critical, the wedge surface gains steepness to achieve the critical taper angle.

Numerical code

We use an improved version of the finite element numerical method described in Fuller et al. (2006a, 2006b). The numerical method accounts for features associated with a subduction wedge, such as accretion of a relatively thin sedimentary layer and flexure of two elastic plates. The subduction process is simulated with a hybrid kinematic-dynamic method in which the subducting crust and mantle of both plates have a prescribed motion, and the crust of the overriding plate can deform in response to body forces and boundary velocities. This method can simulate the deformation of frictional materials, such as sand and rock, and has been verified against analytical solutions (Willett, 1992; Willett and Pope, 2004; Fuller et al., 2006a, 2006b). The numerical method accounts for changes in sediment accumulation rate (compacted sedimentation rate) through time, strain softening/healing and material tracking, after Cassola (2013).

The code obtains the numerical solutions for different parameters over two distinct domains (mechanical and thermo-kinematic domain) (Fig. S1). The domain where mechanical laws apply represents the crust of a deforming subduction zone where sedimentary accretion of incoming sediments is driven by tangential velocities at its base. Tangential velocities decrease toward, and become zero, at the "S" point, which represents the contact point between the subducting slab and continental Moho (Fig. 4). Albeit important for shorter-term processes, elasticity is only considered for the flexural isostatic response to vertical loads and included as an elastic foundation that is calculated by assuming two elastic plates that remain in contact (Fuller, 2006).

Deformations calculated in the mechanical domain use a two-dimensional, mixed finite element Arbitrary Lagrangian-Eulerian method (ALE), during which the velocity and pressure are treated as independent variables (Fullsack, 1995) (Fig. S1a,b). The ALE method combines a semi-fix Eulerian mesh (Fig. S1a) and free Lagrangian markers (Fig. S1b). The Eulerian mesh is fixed along the horizontal position but free on the vertical direction to account for surface processes, and calculate the strain and stresses. The Lagrangian markers are free to move over the Eulerian mesh to compute the velocities and track the internal friction angle (ϕ) and the cumulative second invariant of the strain rate ($\mathrm{E}_{2D}^{\frac{1}{2}}$). The temperature field is calculated on a thermal-kinematic domain using a Eulerian semi-fixed grid that includes as well the mechanical domain and covers the entire model from the base of the lithosphere to the surface (Fig. S1c) (Willett and Pope, 2004).

1 Strain, stress, and temperature

The strain is defined as the second invariant of the deviatoric strain rate ($I'2$). The resulting stress regime for each time step is calculated on the Eulerian mesh using the mean weighted value of the internal friction angle (ϕ) that is stored on the Lagrangian markers of each Eulerian element. Rheologically, the crustal domain is assumed to behave as an incompressible viscous fluid, with a frictional-depended plastic behavior and a thermally-activated viscous behavior. Viscosity is defined as a function of temperature, pressure and stress through the following power-law relationship:

$$\gamma^{\cdot} = A_D(\sigma_d)^n exp\left(\frac{-E_a+V_aP}{RT}\right) \qquad (1)$$

where $\gamma^{\cdot}$ is the strain rate. A_D is the viscosity coefficient and n is the viscosity exponent. E_a is the activation energy, V_a is the activation volume, R is the gas constant, P and T are pressure and temperature. The value of the exponent *n* used in this study is 2.65, which is common in numerical models of the crust (e.g., Willett and Pope, 2004; Ueda et al., 2008). The change in behaviour of the model in time depends on the type of rheology used. For example a value of n < 1 would lessen the impact of thermally activated viscosity and thus increase the similarity among models with different sedimentation rate.

Frictional plastic deformation is calculated using a non-linear viscous formulation that approximates the limit condition associated with a Coulomb yield criterion, defined as:

$$\sigma_y = c\ cos(\phi) + \frac{J_1}{3}sin(\phi) \qquad (2)$$

where *c* is the cohesion of the material, ϕ is the internal angle of friction and J_1 is the first stress invariant. Plastic failure occurs when $\sqrt{J_2'} \geq \sigma^y$, with J'_2 been the second invariant of the deviatoric stress. Then, the effective viscosity in the event of plastic failure is computed as:

$$\mu_{eff} = \frac{c\ cos(\phi)+\frac{J_1}{3}sin(\phi)}{2\sqrt{I_2'}} \qquad (3)$$

Where, I_2' is the second invariant of the deviatoric rate of strain tensor. Under these conditions, the material behaves as an infinitely viscous (rigid) material if $\sqrt{J'_2} < \sigma^y$.

Temperature is determined within the thermal-kinematic domain solving a time-dependent heat transport equation, described in detail in Willett and Pope (2004) that includes conduction, advection, and radiogenic heat production. The code resolves heat advection by a dynamic calculus of the velocity in the mechanical domain, and using a kinematically prescribed velocity elsewhere. The thermal parameters used can be found in Fuller et al. (2006) and an extended description of the equations are in Cassola (2013).

1.1. Strain softening

Strain is accommodated by brittle deformation in the mechanical domain. In nature, this is expressed as a fault zone characterized by an embedded zone of weaker material occurring during deformation and increasing strain (Rutter et al., 2001). A strain softening function in the numerical code reproduces the weakening of the rock with increasing strain (Cassola, 2013). Numerical strain softening reduces the internal friction angle (ϕ) with increasing cumulative strain (Huismans and Beaumont, 2002) and is able to create localized shear zones. The strain rate for each time step, calculated on the Eulerian element, is added to the cumulative strain stored on the Lagrangian marker. The cumulative strain will be used then by the strain softening function to reduce accordingly the internal friction angle stored on the Lagrangian marker (Cassola, 2013).

The strain softening function used in the numerical model is based on the work of Frederiksen and Braun (2001):

$$\phi^* = B\phi + (1 - B)/\mathrm{E}_k \qquad (4)$$

where

$$B = \frac{1}{2}\left[1 - \frac{2}{\pi} arctan\left(\frac{\mathrm{E}_{2D}^{\frac{1}{2}} - \mathrm{E}_{crit}}{\Delta \mathrm{E}}\right)\right] \tag{5}$$

$$\mathrm{E}_{2D}^{\frac{1}{2}} = \int_{t_0}^{t_{tot}} I'_2 dt - \int_{t_0}^{t_{tot}} E_{healing} dt \tag{6}$$

The internal friction angle of the material, ϕ, is weakened to ϕ^* following an arctangent formulation where $\mathrm{E}_{2D}^{\frac{1}{2}}$ is the cumulative second invariant of the deviatoric strain rate ($I'2$) at each time step (6). Three parameters control the weakening method (Frederiksen and Braun, 2001). *Ek* describes the size of weakening from an initial internal friction angle, ϕ, to the weakened internal friction angle, ϕ^*. *Ecrit* defines the amount of cumulative strain at which strength is reduced by 50%. ΔE is the strain interval over which the reduction takes place. The softening parameters have been tuned to get distinct weak shear zones.

1.2. Strain healing factor

Fault zones in nature show strength recovery after a period of inactivity (Yasuhara et al., 2005). We introduce this process in our numerical model by a "healing factor" coefficient that describes how the cumulative strain should recover over time (6).

We define the healing factor, $E_{healing}$, as a constant amount to the strain rate of one order of magnitude smaller than the average strain rate occurring on the last active thrust fault. This amount is subtracted from the total accumulated strain at every time step for each Lagrangian marker (6). In this manner, if no deformation occurs at the Lagrangian element, the total accumulated strain decreases and the element gains in strength again with every timestep as the internal friction angle (ϕ) increases. Contrarily, if deformation occurs, the healing factor becomes neglectable compared to the actual strain rate affecting the element.

2 Sediment accumulation rate

The model adds material from an outside source and there is no mass balance. Model controls on sediment accumulation rates allow the creation of overfilled or underfilled basins. Overfilled conditions are met when high sedimentation rates result in sediments reaching the lower bounding flank of a basin, which in turn determines the fill level. Contrarily, underfilled conditions occur if sediments do not reach one of the two flanks of the basin, as for example when the dynamically calculated subsidence rate is higher than the prescribed sedimentation rate.

The model identifies the lowest point of a depression between two flanks to calculate the corresponding fill height on the basis of the specified sedimentation rate. Points of the Eulerian grid between the flanks that are below the fill height are then advected to the new fill level. The creation of new topography in the basin by the inclusion of the new sediments do not consider sediment compaction by overburden. Sediment rates are thus to be considered as already compacted sediment rates. At each time step, the simulation computes each sediment increment to calculate a new sediment load in the basin and a new isostatic load on the plates.

The sedimentation in the basin always results in a flat stratigraphy at the time of sedimentation, which gets progressively deformed due to increasing isostatic load of further sedimentation and deformation of the accretionary wedge. Isostatic load is recomputed at every sediment filling step. In addition, we introduce horizontal isochronal eulerian lines of markers during the filling of the basin to keep track of the developing basin stratigraphy. Points of these line markers are advected using the velocity field computed at every step. Therefore as the basins deform due to isostatic load or deformation in the basin, the isochrones are also deformed.

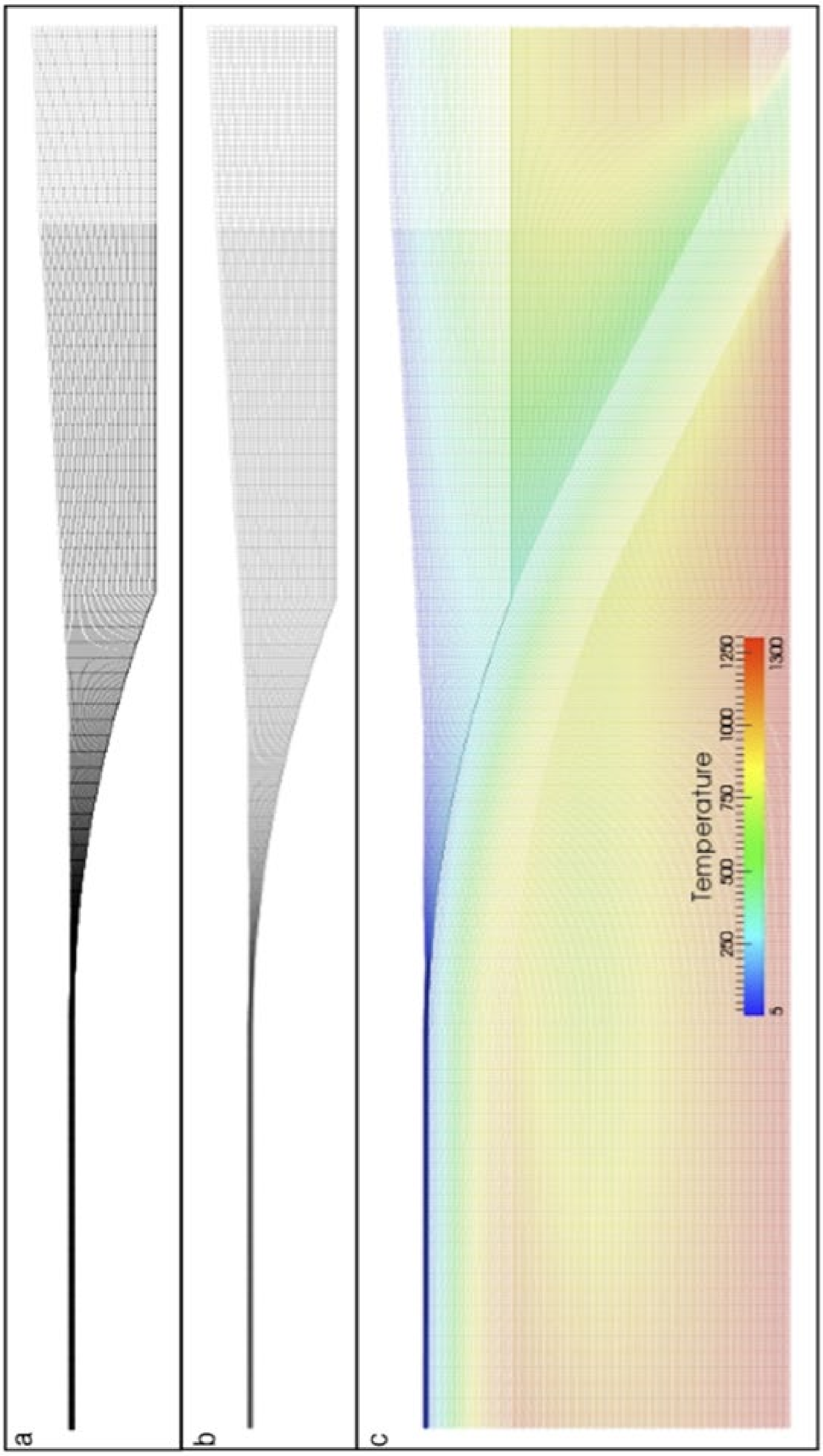

Fig. S1. Arbitrary Lagrangian-Eulerian mesh and thermal mesh. (a) Eulerian mesh where strain, stresses and velocities are calculated. (b) Lagrangian markers used to track material properties and weak zones. Markers advect over the Eulerian mesh responding to the calculated velocity. (c) Thermal mesh on which temperatures are calculated. It extends to the asthenosphere.

Video S2. *Video of preferred model*

https://widgets.figshare.com/articles/12058527/embed?show_title=1

Table S3. *Mechanical and thermal parameters used in the models.*

Mechanical Model		
Parameter	**Description**	**Value**
ρ_c	Lithospheric density	2800 kg/m^3
ρ_m	Mantle density	3300 kg/m^3
ρ_w	Water density	1030 kg/m^3
ϕ	Internal friction angle	27°
ϕ_b	Friction angle between subducting and overriding plate	8°
c	Cohesion	1000 Pa
D	Flexural rigidity	2.4 x 10^{23} N·m
S_α	Slab angle at S point	40°
υ_c	Convergence velocity	35 mm/y
h	Sediment thickness in the subducting plate	3 km
Sed_r	Sedimentation rate	0.5 mm/y
Thermal Model		
Parameter	**Description**	**Value**
H_{sl}	Thickness of the subducting lithosphere	70 km
H_{ol}	Thickness of the overriding lithosphere	80 km
Ma_{lith}	Age of the subducting lithosphere	50 Ma
t_{runup}	Thermal model runup	20 My
$K_{l,a}$	Thermal conductivity (lithosphere, asthenosphere)	2.0, 50.0 W/(m·°K)
T_s	Surface temperature	5 °C
T_a	Asthenospere temperature	1400 °C
A	Heat production	0.85 μW/m^3
c	Specific heat	1200 J/Kg·°K
A_μ	Power-law viscosity coefficient	2.05 Pa^{-n}/Ma
n_μ	Power-law viscosity exponent	2.65
Q	Activation energy	1.7 J/mol

Appendix References

Cassola, T., 2013. Mechanics of forearc basins. ETH Zurich.

Dahlen, F.A., 1984. Noncohesive critical Coulomb wedges: An exact solution. Journal of Geophysical Research 89, 10125–10133.

Davis, D., Suppe, J., Dahlen, F.A., 1983. Mechanics of fold-and-thrust belts and accretionary wedges. Journal of Geophysical Research.

Frederiksen, S., Braun, J., 2001. Numerical modelling of strain localisation during extension of the continental lithosphere. Earth and Planetary Science Letters 188, 241–251.

Fuller, C.W., 2006. Controls on the Structural Morphology and Subduction-thrust Seismicity of Accretionary Margins. University of Washington.

Fuller, C.W., Willett, S.D., Brandon, M.T., 2006a. Formation of forearc basins and their influence on subduction zone earthquakes. Geology 34, 65–68.

Fuller, C.W., Willett, S.D., Fisher, D., Lu, C.Y., 2006b. A thermomechanical wedge model of Taiwan constrained by fission-track thermochronometry. Tectonophysics 425, 1–24.

Fullsack, P., 1995. An arbitrary Lagrangian-Eulerian formulation for creeping flows and its application in tectonic models. Geophysical Journal International 120, 1–23.

Huismans, R.S., Beaumont, C., 2002. Asymmetric lithospheric extension: The role of frictional plastic strain softening inferred from numerical experiments. Geology.

Rutter, E.H., Holdsworth, R.E., Knipe, R.J., 2001. The nature and tectonic significance of fault-zone weakening: an introduction. Geological Society, London, Special Publications. doi:10.1144/gsl.sp.2001.186.01.01

Ueda, K., Gerya, T., Sobolev, S.V., 2008. Subduction initiation by thermal–chemical plumes: Numerical studies. Phys. Earth Planet. Inter. 171, 296–312.

Wang, W.-H., Davis, D.M., 1996. Sandbox model simulation of forearc evolution and noncritical wedges. J. Geophys. Res. 101, 11329–11339.

Willett, S.D., 1992. Dynamic and kinematic growth and change of a Coulomb wedge, in: McClay, K.R. (Ed.), Thrust Tectonics. Springer Netherlands, Dordrecht, pp. 19–31.

Willett, S.D., Pope, D.C., 2004. 7. Thermo-Mechanical Models of Convergent Orogenesis: Thermal and Rheologic Dependence of Crustal Deformation, in: Rheology and Deformation of the Lithosphere at Continental Margins.

Yasuhara, H., Marone, C., Elsworth, D., 2005. Fault zone restrengthening and frictional healing: The role of pressure solution. Journal of Geophysical Research: Solid Earth 110. doi:10.1029/2004JB003327